University of Southampton
Department of Physics

# Magnetic studies of thallium-based high temperature superconductors

by

Stephan Venzke

Thesis submitted for examination for the degree of
Master of Philosophy

September 1992

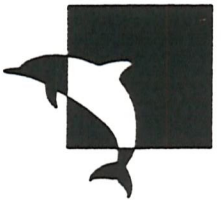


"... According to the known laws of lines of force about magnets and currents, we are now having to inquire into the physical connection of these vortices with currents, while we are still in doubt as to the nature of electricity. ..."

*James Clerk Maxwell, 1861*

UNIVERSITY OF SOUTHAMPTON

ABSTRACT

FACULTY OF SCIENCE

DEPARTMENT OF PHYSICS

Master of Philosophy

# MAGNETIC STUDIES OF THALLIUM-BASED HIGH TEMPERATURE SUPERCONDUCTORS

by Stephan Venzke

An investigation has been carried out into the magnetic properties of thallium-based high temperature superconductors belonging to the homologous series $Tl_2Ba_2Ca_{n-1}Cu_nO_{2n+4}$ for $n = 2, 3, 4$.

First, the superconducting properties of differently prepared samples have been studied. The investigated samples were prepared in six separate series. Each series contained of samples which were annealed under different conditions. Magnetic hysteresis measurements were performed and the critical current density was determined from the width of the magnetic hysteresis loops. Comparing the results of these experiments with the powder x-ray and neutron diffraction data collected on the investigated samples, the critical current density was found to increase with increasing hole concentration on the copper-oxygen planes. Several possible explanations for this behaviour have been discussed. The transition temperature showed an inverse parabolic dependence as a function of the hole concentration on the copper-oxygen planes. This is consistent with the behaviour modelled.

Second, the mechanism of flux motion in $Tl_2Ba_2Ca_2Cu_3O_{10+\delta}$ has been investigated using various methods: The vortex pinning force was measured as a function of the applied magnetic field, variable sweep-rate experiments and relaxation measurements were performed and the temperature dependence of the critical current density was examined. The results showed that the Anderson-Kim theory of thermally activated flux motion could describe flux motion in $Tl_2Ba_2Ca_2Cu_3O_{10+\delta}$ at fixed values of the temperature and applied magnetic field, but failed to describe the temperature and field dependence of the critical current.

# Acknowledgements

First of all, I am particularly indebted to the German National Scholarship Foundation, without whose support it would not have been possible for me to spend this wonderful year here in England. The encouragement and assistance of Prof. W. Press and Prof. M. Skibowski during the administrative process is also greatly appreciated.

I am grateful to my supervisor Dr. P. A. J. de Groot for his guidance and advice throughout this research. Special thanks are due to Professor D. J. Newman, Dr. C. Beduz, Dr. M. T. Weller, Dr. M. Ousséna and Dr. Y. Ren for all their helpfulness and patience in many interesting discussions. My deepest thanks go also to Darren Ogborne, who I had the pleasure of working with. They will never forget the thallium team. Thanks too to the technicians, not only for their technical support but especially for all the enthusiasm that they put into the X-mas party, the treasure hunt and the barbecue. Last but not least, the following deserve a very special mention: Stephen, Tim, Simon and Greg ! They made me, a bloody foreigner, feel at home in England. Thank you very much guys !!!

Finally, I would like to thank everyone who has helped me in any way during the course of this work – your name may have been unintentionally omitted here, but you have not been forgotten !

# Contents

# Chapter 1

# Introduction

## 1.1 Historical survey

The story of this work began more than 80 years ago when Kamerlingh Onnes discovered in Leiden (Netherlands) that on cooling mercury the resistance dropped suddenly to zero at 4.2 Kelvin instead of decreasing smoothly to a finite value as expected [1].

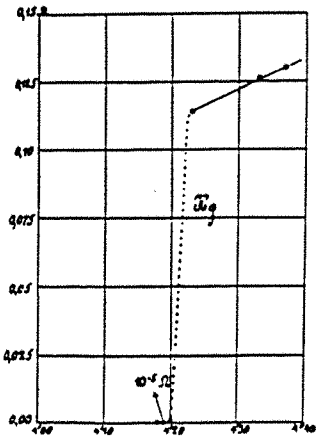

Figure 1.1: *Original measurement of Kamerlingh Onnes.*

This phenomena was named *superconductivity* and first interpreted by Kamerlingh Onnes as a quantum phenomena leading to a rapid decrease of the scattering probability with decreasing temperature [2]. But noticing that

the ratio between the resistance in normal metals and in superconductors is many orders of magnitude he gave up premature theorizing and concentrated on experiments. He immediately had in mind to produce strong magnetic fields without dissipation of Joule heat. It was a great disappointment for him that magnetic fields of a few hundred oersted were found to destroy superconductivity. He found also that there was a maximum current that could flow in the material without resistance. Lots of research has been done since Onnes' discoveries but the maximum current and the relatively low transition temperature between the superconducting and normal state are still limiting the applications of superconductors.

The first successful microscopic explanation of superconductivity was delivered in 1957 by Bardeen, Cooper and Schrieffer (BCS) [3]. Almost 30 years later, in April 1986, George Bednorz and Alex Müller from the IBM laboratories in Rüschlikon confirmed superconductivity in layered cuprates [4]. Before this date the highest observed transition temperature was found in niobium-germanium to be 23 K. A selection of the new High Temperature Superconductors (hereafter referred to as *HTS*) and their transition temperatures is shown in Table 1.1.

| | $T_c$ | year |
|---|---|---|
| $Ba_xLa_5Cu_5O_5$ | 30 K | 1986 |
| $(LaSr)_2CuO_4$ | 38 K | 1986 |
| $YBa_2Cu_3O_7$ | 94 K | 1987 |
| $Bi_2Sr_2CaCu_2O_{8+\delta}$ | 83 K | 1988 |
| $Bi_2Sr_2Ca_2Cu_3O_{10+\delta}$ | 110 K | 1989 |
| $Tl_2Ba_2CaCu_2O_{8+\delta}$ | 110 K | 1988 |
| $Tl_2Ba_2Ca_2Cu_3O_{10+\delta}$ | 128 K | 1988 |
| $Pb_2Sr_2RCu_3O_8$ | 70 K | 1988 |
| $Sr_{0.85}Nd_{0.15}CuO_2$ | 40 K | 1991 |

Table 1.1: *Selection of HTS, their transition temperature and the year of their discovery.*

After 1986 an unparalleled explosion of research activity throughout the world started but a satisfying theory to explain superconductivity in this new cuprates is still lacking.

## 1.2 Magnetic properties of superconductors

Superconducting materials can be divided into two types:

A *type I superconductor* below $T_c$ will completely exclude an externally applied magnetic field up to a critical field $H_c(T)$ and shows reversible behaviour across the range $0 < H_{applied} < H_c$. The final state of the sample is only dependent on the field and temperature, and not on the previous history of the sample. This is the Meissner-Effect. Like Kamerlingh Onnes already found there is a maximum current that the superconductor can carry before a measurable resistance appears. In the case of simple type I superconductors this maximum arises because the flowing current generates an associated magnetic field at the surface of the superconductor which must not exceed the critical field $H_c$.

The behaviour of *type II superconductors*, including the HTS, is quite different. The material shows reversible behaviour up to a field $H_{c_1}$. Above this field a magnetic field penetrates the sample in the form of a hexagonal lattice of flux lines containing flux quanta $\Phi = h/2e$ [5]. These flux lines consist of a normal core and are surrounded by a vortex of supercurrent which decays exponentially over a certain distance. In this mixed state the material is still on the whole diamagnetic up to a field $H_{c_2}$, but the magnetic behaviour may be irreversible and show hysteresis. This is due to flux which is trapped in the sample by several pinning centres, such as dislocations in the crystal lattice, non-superconducting impurities or grain boundaries. The amount of pinning in the sample affects the maximum current that can flow in the sample before measurable resistance appears. That is because it prevents flux motion which is caused by the Lorentz force on the flux lines generated by a current flowing in the sample. Motion of flux means a dissipation of energy and hence causes an effective resistance to current flowing in the sample. In the presence of pinning centres the Lorentz force is counteracted by a pinning force $F_p$, and, at zero temperature, a voltage is observed only if J exceeds the critical current density $J_{c_0}$. At $T > 0$, there is also a finite probability for thermally activated vortex depinning.

## 1.3 Thallium-based superconductors

Amongst the HTS the highest critical temperatures are found for the thallium-based cuprates. In the Tl-Ba-Ca-Cu-O system, high temperature superconductivity was discovered by Sheng and Hermann in March 1988 [6]. Two main homologous series of compounds exist: the single thallium layer structures of general composition $TlBa_2Ca_{n-1}Cu_nO_{2n+3}$ $(n = 1, 2, 3, 4, 5)$ and the double layer compounds of general formula $Tl_2Ba_2Ca_{n-1}Cu_nO_{2n+4}$ $(n = 1, 2, 3, 4)$ [6, 7, 9]. In June 1988 Parkin et al.[10] reported a method for the synthesis of $Tl_2Ba_2Ca_2Cu_3O_{10+\delta}$ which exhibited zero resistance and diamagnetism below a temperature of 125 K. Recently Liu,Tallon and Edwards [11] reported improvements of $T_c$ up to 128 K obtained by low temperature annealing of the sample in controlled oxygen partial pressure. The origins of these $T_c$-improvements are not clear but the authors suggest it is likely to be a result of a change in the oxygen stoichiometry.

## 1.4 Intention of this work

As part of the collaboration between the Cryogenics, Chemistry and Physics Departments of the University of Southampton, several series of the double layer compounds $Tl_2Ba_2Ca_2Cu_3O_{10+\delta}$ (hereafter referred to as Tl-2223), $Tl_2Ba_2Ca_1Cu_2O_{8+\delta}$ (Tl-2212) and $Tl_2Ba_2Ca_3Cu_4O_{12+\delta}$ (Tl-2234) were prepared under different conditions by D.M.Ogborne in the Chemistry Department. He investigated the effects of changes in the oxygen stoichiometry in some of the series on their structure as determined by powder neutron diffraction. The main purpose of this work was to investigate how far changes in the oxygen stoichiometry as a result of the different annealing procedures used, influence the critical current density and the transition temperature of Tl-2223, Tl-2212 and Tl-2234. It is very important for applications to improve the critical current density of these materials, which are especially useful because of their high transition temperature. Here the effect of different preparation procedures on the intrinsic pinning of the flux lines was investigated in order to find new methods to produce thallium-based high temperature superconductors which are able to carry current densities of the order of $10^5 A/cm^2$ at relatively high temperatures as required for many applications. Details of the preparation and the resulting superconducting proper-

ties are shown in Chapter 4. Apart from these studies of differently prepared samples, studies of the sweep-rate, temperature and field dependence of the critical current density were made on one specific Tl-2223 sample. The theoretical background for this will be provided in Chapter 2. Chapter 5 presents the experimental results and conclusions of the work done in this field.

# Bibliography


[1] H. Kamerlingh Onnes, Akad. van Wetenschappen (Amsterdam) **14**, 113 (1911)

[2] C. J. Gorter, Rev. Mo. Phys., **36**, 1 (1964)

[3] J. Bardeen, L. N. Cooper and J. R. Schrieffer, Phys. Rev. **106**, 162 (1957) and Phys. Rev. **198**, 1175 (1957)

[4] J. G. Bednorz and K. A. Müller, Z. Phys. B **64**, 189 (1986)

[5] A. A. Abrikosov, Phys. Chem. Solids. **2**, 199 (1957)

[6] Z. Z. Sheng and A. M. Hermann, Nature **332**, 138 (1988)

[7] S. Iijima, T. Ichihashi, Y. Shimakawa, T. Mamako and Y. Kubo, Japanese J. Applied Physics **27**, L 1054 (1988)

[8] S. Kawashima, O. Ihove and S. Adach, Japanese J. Applied Physics **29**, L 900 (1990)

[9] D. M. Ogborne, M. T. Weller, P. C. Lanchester, C. Grovenor and L. Romano, Superconducting Science and Technology **5**, 78 (1992)

[10] S. S. P. Parkin, V. Y. Lee, E. M. Engher, A. I. Nazzal, T. C. Huang, G. Gorman, R. Savoy and R. Beyers, Phys. Rev. Lett. **60**, 2539 (1988)

[11] R. S. Liu, J. L. Tallon and P. P. Edwards, Physica C **182**, 119 (1991)

# Chapter 2

# Theoretical background of the critical current

## 2.1 Introduction

The critical current is the superconducting property to which main attention is drawn in this work. Therefore the following chapter will provide the necessary theoretical information about it. First, it will be explained why the current that can be carried by a superconductor without dissipation of energy is limited. Second, the Anderson-Kim model [1, 2, 3] and a few more recent models [8] to [19] which all claim to describe the motion of the flux lines will be presented. A model proposed by C. P. Bean in 1962 [4] describes the connection between the critical current and the magnetisation of the sample. How this is possible is shown in this chapter as well. Like most physical quantities the critical current is dependent on certain parameters. The last three sections of this chapter are about existing theories of the sweep-rate-, temperature-, and field dependence of the critical current and give a theoretical derivation of the correlation between magnetic hysteresis and magnetic relaxation. How far these theories are applicable to Tl-based superconductors shall then be investigated experimentally in chapter 5.

## 2.2 Theories of flux motion

### 2.2.1 The zero-temperature critical current

Vortices in type II superconductors in the mixed state, $H_{c_1} < H_{applied} < H_{c_2}$, are pinned at zero-temperature. This still remains the case when a current is flowing until the current is such that the Lorentz force

$$\mathbf{F_L} = \mathbf{J_0} \times \mathbf{\Phi_0} \tag{2.1}$$

which tends to move the vortex at right angles to the direction of the current flow, exceeds the pinning force $F_P$ which tries to maintain the flux lines at rest. This value is referred to as the zero-temperature critical current, usually expressed as the critical current density $J_{c_0}$ in $A/cm^2$.

For $J > J_{c_0}$ the driving force is large enough to move the vortices. Their motion is subject to a viscous drag, giving rise to dissipation that shows up as a macroscopic resistivity at a right angle to the vortex motion. Following Bardeen and Stephen [5] the dissipation process is due to the current passing through the normal vortex core. If the vortices were not moving, the current would flow around the core and there would be no dissipation. Furthermore a detailed theoretical description was supplied by Anderson [6]. Conductance without loss is therefore only possible if the vortices are prevented from moving. They may be pinned by, for example, dislocations in the crystal lattice, non-superconducting impurities or at grain boundaries. All these pin the vortices by providing a site such that the free energy of the vortex is lowered when the vortex is sitting on the pinning centre. A certain energy is needed to unpin the vortex from this potential energy well. This situation is shown in figure 2.1 (a).

If a driving force, for example a current or field gradient, is now applied to the system, the pinning potential tilts in the direction of the internal field gradient. If the stress is great enough, there will no longer be minima in the pinning potential and the vortices become unpinned, as shown in figure 2.1(b). The current at which this occurs is the zero-temperature critical current $J_{c_0}$.

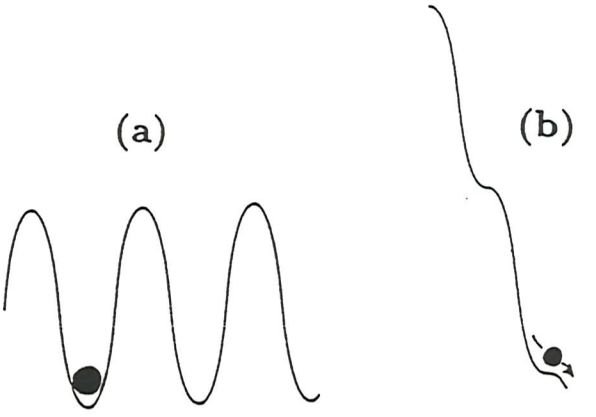


Figure 2.1: *Potential energy well for* $T = 0$ *and (a)* $J_0 = 0$, *(b)* $J_0 > 0$.

### 2.2.2 General formalism of stress-assisted thermal activation of flux motion

The *general* character of the formalism is restricted by some assumptions: First it is assumed that some entities sit at the bottom of a periodic potential well of the depth $U_0$. $U_0$ is the difference in the Gibbs Function of the system between the state when the entity is in the well and the state when it is moved away from it. Second the energy $U_0$ is assumed to be constant and third the entities shall move independently.

In the absence of any imposed stress the entities can, due to thermal activation, hop out of the well by a rate which is given by

$$R = \Omega_0 \exp\left(-\frac{U_0}{k_B T}\right) \tag{2.2}$$

where $\Omega_0$ is the average attempt frequency with which the entity tries to escape from the well. It is hard to estimate and usually taken around $10^{10} Hz$. As the hopping rates are the same in all directions no net motion of the entity is observed. When a stress is imposed in such a way as to favour hopping in one direction, which now can be identified as the forward direction, the rates of the forward, $R_f$, and backward, $R_b$, hopping become

$$R_f = \Omega_0 \exp\left(-\frac{U_0 - \Delta W}{k_B T}\right) \tag{2.3}$$

and

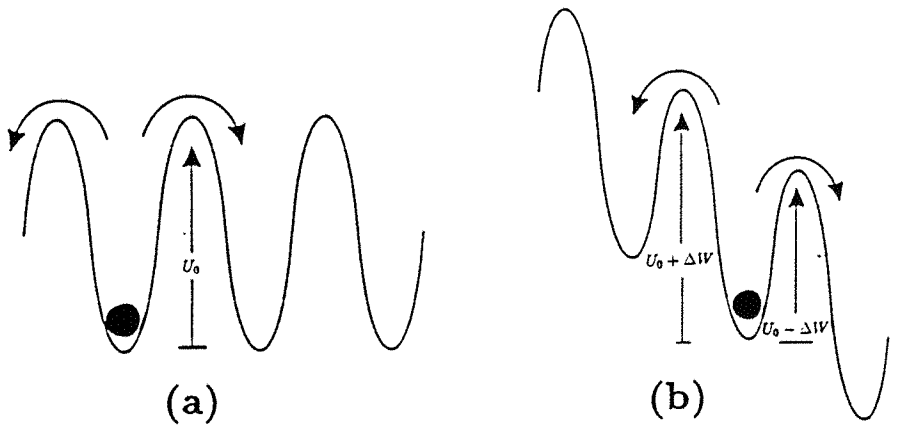


Figure 2.2: *Potential energy well during an imposed stress.*

$$R_b = \Omega_0 \exp\left(-\frac{U_0 + \Delta W}{k_B T}\right) \tag{2.4}$$

where $\Delta W$ is the work done by the imposed stress in moving the entity from the equilibrium position at the bottom of the well to the next equilibrium position (figure 2.2).

There is now a net forward rate of hopping given by the difference between these two expressions

$$R_{net} = 2\Omega_0 \exp\left(-\frac{U_0}{k_B T}\right) \sinh\left(\frac{\Delta W}{k_B T}\right). \tag{2.5}$$

In a superconductor the moving entities are bundles of flux, which need not necessarily be single quantized flux lines. Taking the magnetic field directed along the z-axis, the motion of the flux lines along the field gradient in the x-direction generates an electric field in the y-direction which is according to the Maxwell equation $\frac{\partial \mathbf{B}}{\partial t} = -\nabla \times \mathbf{E}$ given by

$$E = vB \tag{2.6}$$

where $v$ is the average velocity of the moving flux lines. If we define $\delta x$ as the distance over which the flux lines move in each hop, we obtain the average velocity

$$v = R_{net}\delta x \tag{2.7}$$

and electrical field is therefore given by

$$E = R_{net}\delta x B = 2\delta x B\Omega_0 \exp\left(-\frac{U_0}{k_B T}\right)\sinh\left(\frac{\Delta W}{k_B T}\right). \tag{2.8}$$

Conservation of flux requires a continuity equation which can be found by rewriting the above mentioned Maxwell equation for the case of the above chosen directions:

$$\frac{\partial B}{\partial t} = \nabla \cdot \left[\left(\frac{\nabla B}{|\nabla B|}\right) 2\delta x \Omega_0 B \exp\left(-\frac{U_0}{k_B T}\right)\sinh\left(\frac{\Delta W}{k_B T}\right)\right]. \tag{2.9}$$

This partial differential equation can not be solved analytically. But it is possible to consider two cases which lead to simplifications:

(i) $\underline{\Delta W \gg k_B T}$:

that is either at high levels of imposed stress or at low temperatures. For large $x$, $\sinh(x) \simeq \frac{1}{2}\exp(x)$. Thus the net rate of hopping becomes

$$R_{net} = \Omega_0 \exp\left(-\frac{U_0 - \Delta W}{k_B T}\right). \tag{2.10}$$

(ii) $\underline{\Delta W \ll k_B T}$:

that is either at low levels of imposed stress or at high temperatures. When $x$ is small, $\sinh(x)$ is approximately equal to $x$ and the net rate of hopping becomes

$$R_{net} = 2\Omega_0 \left(\frac{\Delta W}{k_B T}\right)\exp\left(-\frac{U_0}{k_B T}\right). \tag{2.11}$$

The first case occurs in what is known as the *flux creep regime* which will be described below (section 2.2.3) in the Anderson-Kim model. In the latter case flux motion can occur for small driving forces. This is known as the *thermally assisted flux flow (TAFF) regime*, also discussed later in section 2.2.4.

### 2.2.3 The Anderson-Kim model

In 1962 Anderson published his theory of flux creep in hard superconductors [1]. He proposed that the mechanism of flux creep is the thermally activated

motion of bundles of flux lines over free energy barriers which are due to the pinning effect of inhomogeneties, dislocations or other physical defects. This is superpositioned on the motion caused by the Lorentz force. As one can now see, all his assumptions about this mechanism are included in the formalism derived in the previous paragraph. For classical superconductors only the limiting case $\Delta W \gg k_B T$ was of interest. Therefore Anderson and later Beasley et al. [4] only treated this situation. It leads to a continuity equation

$$\frac{\partial B}{\partial t} = \nabla \cdot \left[ \left( \frac{\nabla B}{|\nabla B|} \right) \delta x \Omega_0 B \exp \left( -\frac{U_0 - \Delta W}{k_B T} \right) \right] \tag{2.12}$$

as can be seen from equation 2.9 and 2.10.

As Anderson already emphasized his flux creep theory is an extremely rough theory of only one of many possible regimes of behaviour of the hard superconductor. He neglected important factors such as changes of the free energy with current or field, shape factors of the flux bundles or details of interactions between them. But nevertheless the results were surprisingly accurate for Kim's measurements [2].

After the discovery of HTS in 1986 extensions to Anderson's model were made by Griessen et al. [8, 6, 7] to avoid the limitation $\Delta W \gg k_B T$ which seemed to be invalid for high-$T_c$ superconductors. Their model, based on thermally activated flux creep, assumes a different pinning potential, which considers only two pinning regions. With these assumptions equation 2.9 can be solved numerically for all $\Delta W / k_B T$ values.

### 2.2.4 Thermally assisted flux flow (TAFF)

The importance of TAFF for high temperature superconductors was first pointed out by Dew-Hughes [11]. To define $U_0$ and $\Delta W$ he supposed that flux is pinned in the superconductor by non-superconducting particles whose number density is $N_p$ per unit volume. $U_0$ is the difference in Gibbs Function when a flux line intersects a particle and when it is out of the particle. $U_0$ is a function of both the magnetic induction B and the temperature T. Provided that the induction is sufficiently large so that each pinning particle is intersected by a flux line, then the pinning energy per unit volume is $U_0 N_p$ and therefore the pinning force per unit volume is

$$J_{c_0} B = \frac{U_0 N_p}{\delta x} \tag{2.13}$$

where $J_{c_0}$ is what the critical current density would be in the absence of any flux creep or in other words the critical current density just before creep.

The actual current flowing exerts a Lorentz force

$$\mathbf{F_L} = \mathbf{J} \times \mathbf{B} \tag{2.14}$$

per unit volume on the flux lattice, where $J$ is the actual current density and less than $J_{c_0}$. The work done if a volume $\delta v$ of flux lattice moves over a distance $\delta x$ is

$$\Delta W = JB\delta v\delta x. \tag{2.15}$$

When a flux line becomes unpinned it will not move alone but neighbouring flux lines will move along with it. It is reasonable to assume that the entire volume of flux lattice associated with one pinning centre will on average move each time a flux line is unpinned. This leads to:

$$\delta v = \frac{1}{N_p} \tag{2.16}$$

This volume of lattice, which is the equivalent of Anderson's flux bundles will move until it intersects the next particle. The distance moved will thus be one inter-flux-line spacing:

$$\delta x = a_0 \tag{2.17}$$

Therefore

$$\Delta W = JB\delta v\delta x = \frac{JBa_0}{N_p} = U_0 \frac{J}{J_{c_0}} \tag{2.18}$$

If we consider now the case $\Delta W \gg k_B T$, as Beasley did [4], and use equations 2.8 and 2.10 we find

$$E = a_0 \Omega_0 B \exp\left(-\frac{U_0 - \Delta W}{k_B T}\right) = a_0 \Omega_0 B \exp\left(\frac{U_0 (J - J_{c_0})}{J_{c_0} k_B T}\right) \tag{2.19}$$

and

$$J = J_{c_0}\left(1 + \frac{k_B T}{U_0}\ln\frac{E}{a_0 B\Omega_0}\right). \tag{2.20}$$

This result means that in this case $E(J)$ increases exponentially with $J$ (flux creep). But if we consider $\Delta W \ll k_B T$ and use equations 2.8 and 2.11 we get

$$E = 2a_0\Omega_0 B\frac{U_0}{k_B T}\frac{J}{J_{c_0}}\exp\left(-\frac{U_0}{k_B T}\right) \tag{2.21}$$

where $E(J)$ is linear. In this regime of thermally assisted flux flow (TAFF) an electrical resistivity

$$\rho_f = \frac{E}{J} = 2a_0\Omega_0\frac{U_0}{k_B T J_{c_0}}B\exp\left(-\frac{U_0}{k_B T}\right) \tag{2.22}$$

occurs.

P. H. Kes et al. [12] support the importance of thermally assisted flux flow (TAFF) in high temperature superconductors. They obtain equation 2.9 for this limit where $2\sinh\left(\frac{\Delta W}{k_B T}\right) \simeq \frac{2\Delta W}{k_B T}$. In the case of a slab in the $y-z$ plane equation 2.9 becomes

$$\frac{\partial B}{\partial t} = \frac{\partial}{\partial x}\left(D\frac{\partial B}{\partial x}\right) \tag{2.23}$$

where

$$D = 2a_0\Omega_0\frac{U_0}{k_B T\mu_0 J_{c_0}}B\exp\left(-\frac{U_0}{k_B T}\right) \tag{2.24}$$

is related to the flux flow density D defined by Beasley [4] and is analogous to the diffusion constant in a diffusion problem. It is obvious that D depends on $B$ and $T$ and is further influenced by the pinning characteristics. However, since $J$ is taken to be small in the $\Delta W \ll k_B T$ regime, $B$ is almost constant. Kes et al. show that it is therefore possible to replace $D$ by its constant value $D_0 = D(B_0)$. A comparison with equation 2.22 shows that the flux flow resistivity $\rho_f$ can be expressed as

$$\rho_f = \mu_0 D_0. \tag{2.25}$$

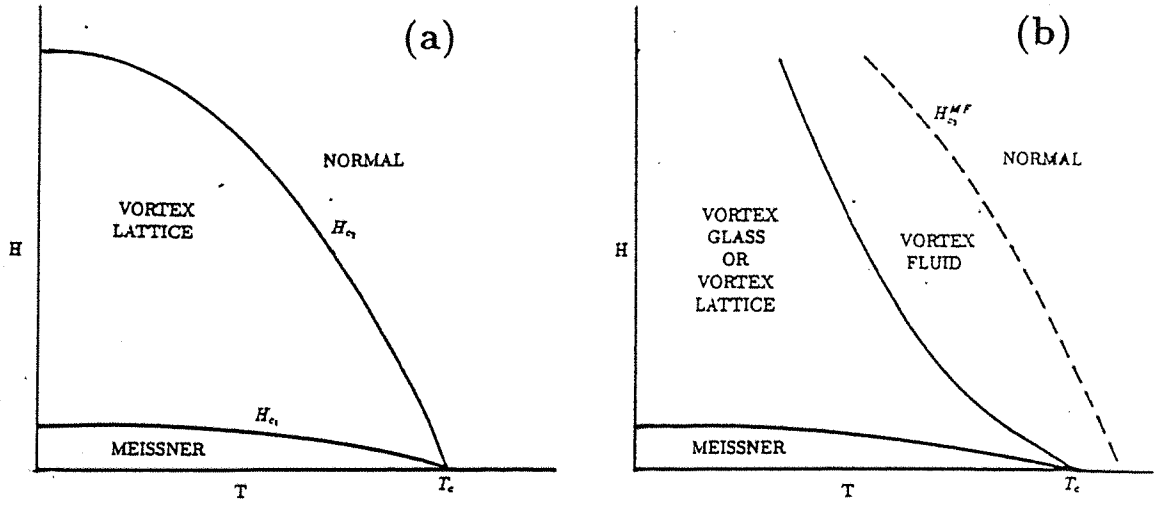


Figure 2.3: *Schematic phase diagram of (a) a conventional type II superconductor and (b) a high temperature superconductor.*

### 2.2.5 Possible vortex phases in the mixed state

As seen at the end of the last section the question regarding the mixed state is whether a high temperature superconductor looses its defining property, a vanishing ohmic resistance, due to thermally assisted flux flow or not.

According to the theory of Fisher et al.[13, 14] pinning of vortices due to impurities or other defects destroys the long range correlations of the vortex lattice, probably replacing it with a new distinct thermodynamic phase, the vortex-glass phase, that has spin-glass like off-diagonal long range order and is truly superconducting. This is in contrast to conventional theories of flux creep [1] to [12] which have generally neglected the question of long range phase coherence beyond the length scale where the lattice correlations are destroyed.

Figure 2.3 shows a comparison of schematic phase diagrams of a conventional type II superconductor and of a high temperature superconductor.

The conventional type II superconductor excludes a magnetic field up to $H_{c_1}$ then enters the vortex state and when the field exceeds $H_{c_2}$ the material becomes normal. In the case of HTS materials the vortex-glass phase is separated from the vortex-liquid by a second order phase transition. In contrast

to the vortex-glass, the vortex-liquid phase lacks long range superconducting order. It is characterized by a finite linear resistance and the critical current density is zero.

The expression for the dependence of the electric field on the current which has been put forward by Fisher et al. is:

$$E \propto \exp\left(-\left(\frac{J_c}{J}\right)^{\mu}\right); \mu \leq 1 \tag{2.26}$$

This has been derived in the Meissner phase (vortex nucleation by thermal fluctuation) and in the 3D glass region (applicable to $YBa_2Cu_3O_{6+\delta}$). However, these regimes are inapplicable to the experiments of this work on $Tl_2Ba_2Ca_{n-1}Cu_nO_{2n+4}$ materials.

A similar result was obtained in the theory of collective flux creep of Feigl'man et al. [13, 14, 15, 16] and independently by Nattermann [19]. Kes et al. [12] supposed that at $J \ll J_c$ the energy barrier $U(J)$ tends to some constant and so the flux relaxation is governed by the conventional linear diffusion equation 2.23 with the diffusion constant

$$D \propto \exp\left(-\frac{U_0}{k_B T}\right). \tag{2.27}$$

In contrast to this Feigl'man showed that the energy $U(J)$ grows at $J \ll J_c$ as $J^{-\mu}$ with $\mu \leq 1$, when the vortex lattice is described as an elastic object. This means the absence of usual linear diffusion ($D \to 0$ at $J \to 0$) and results in an I-V curve of the form $V \propto \exp\left(-\frac{A}{J^{\mu}}\right)$ similar to equation 2.26.

## 2.3 The Bean model

In 1962 Charles Bean proposed a relation between the critical current density and the magnetisation measured in magnetic hysteresis loops [4]. The basic assumption of his model is that if an external magnetic field is applied to a superconducting sample then the shielding currents $J$, which flow in the sample to exclude the field, are always the maximum currents that can flow in the material, i.e. the critical currents $J_c$, or zero.

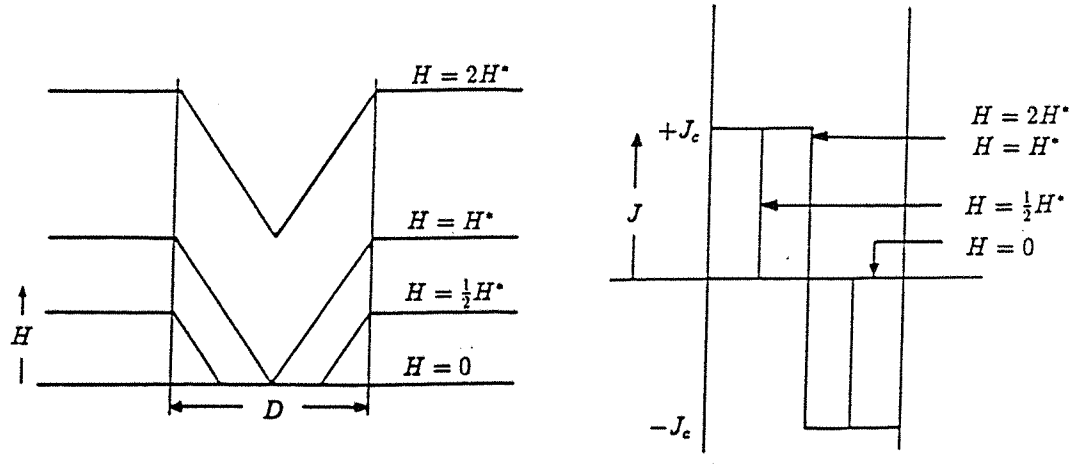


Figure 2.4: *Field profile and current density during a magnetic field increase in a slab sample of a type II superconductor, as given by the Bean model.*

Bean assumed furthermore that this current is independent of, or varies only slowly with, the magnetic field. These assumptions result in a field profile as shown in figure 2.4 for the case of a slab sample.

When the field exceeds $H_{C_1}$ flux penetrates into the sample for a small distance. Due to pinning centres this penetration does not lead to a uniform distribution over the whole sample. The field gradient is assumed to be constant. It is maintained by the screening currents. At a field $H = H^*$ the sample is fully penetrated and for fields greater than $H^*$ the field inside the sample increases.

Most authors refer to a sample in this state as being in the *critical state*, which is the definition used in this work. The importance of the Bean model for this work is that it allows us to deduce the current flowing in a sample from magnetic hysteresis experiments. Figure 2.5 shows the field profile within a slab superconductor at four different points on a magnetic hysteresis loop, according to the Bean model.

In figure (a) the external field has just reached $H^*$ and the sample is saturated with flux. The situation after a further increase of the external field to $H = 2H^*$, which is taken here as the maximum value, is shown in

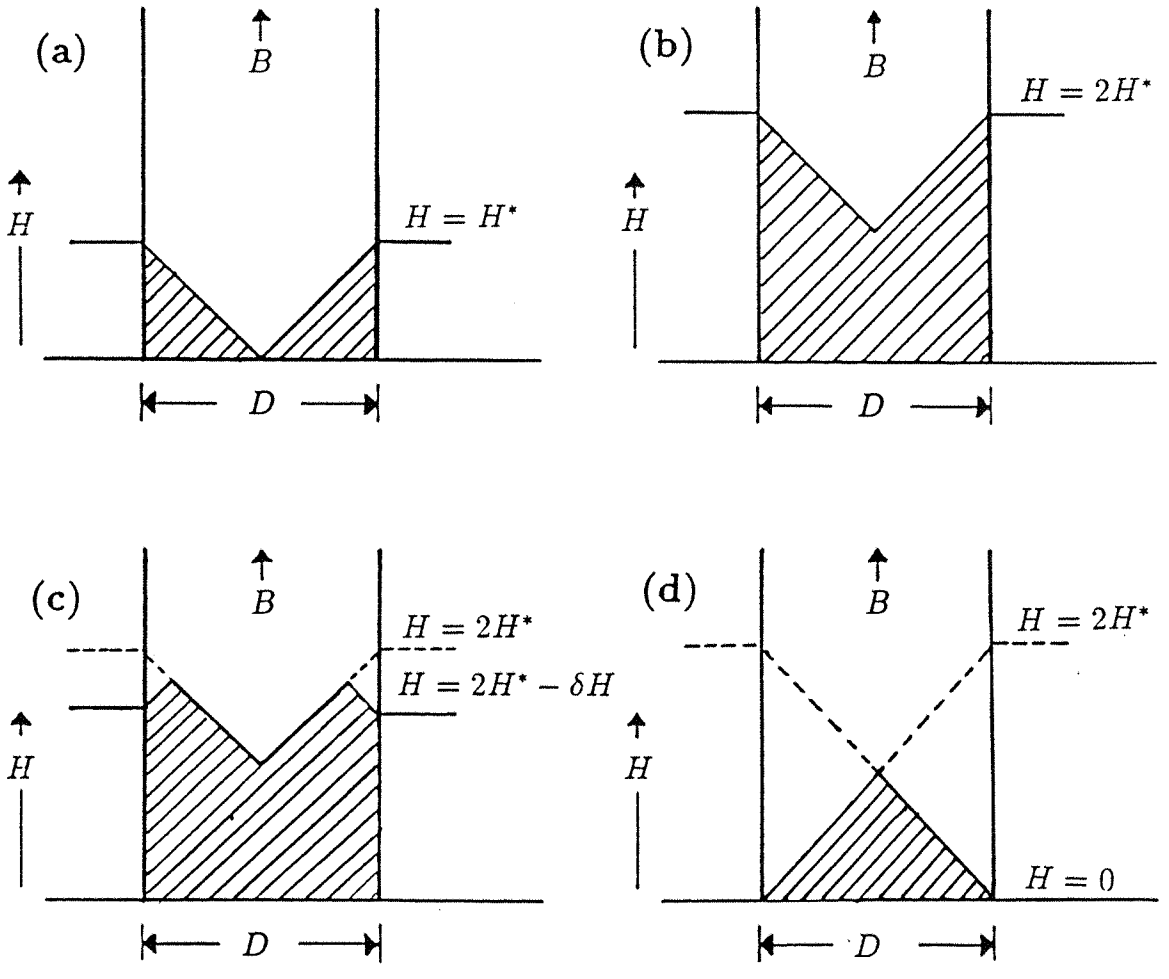


Figure 2.5: *Field profile in a slab sample of a type II superconductor at four points on a magnetic hysteresis loop, according to the Bean model.*

figure (b). In figure (c) the external field has been decreased a little. This leads to a local reversal of the field gradient and screening currents in the sample at the edges. The external field has been reduced to zero in figure (d) but flux remains in the sample as the screening currents continue to flow.

The width of a magnetic hysteresis loop can be used to calculate the critical current density.[1]

Now,

$$\mathbf{B} = \mathbf{H} + 4\pi\mathbf{M} \tag{2.28}$$

where $B$ is the local field inside the sample. We can rearrange to obtain

$$4\pi\mathbf{M} = \frac{1}{V}\int_V (\mathbf{B} - \mathbf{H})\, dV. \tag{2.29}$$

Following the conditions of the experiments in this work we consider now a cylindrical sample which is fully penetrated. The Maxwell-equation

$$\nabla \times \mathbf{B} = 4\pi\mathbf{J_c} \tag{2.30}$$

can be simplified if we take $\mathbf{B}$ directed along the symmetry-axis

$$\mathbf{B} = B(r)\mathbf{k} \tag{2.31}$$

where $r$ is the distance from the symmetry-axis. Then we have

$$\frac{\partial B}{\partial r} = 4\pi J_c. \tag{2.32}$$

Solving this equation we get

$$B(r) = 4\pi J_c r + b. \tag{2.33}$$

The condition $B(R) = H$, where $R$ is the radius of the cylinder gives

$$b = H - 4\pi J_c R \tag{2.34}$$

and therefore

[1]The measurements done in this work provide the magnetisation $M$ per unit volume in units of the **emu**-system at an external field $H$. Therefore the following derivation is not done in **SI**-units.

$$B(r) = 4\pi J_c (r - R) + H. \tag{2.35}$$

Using equation 2.29 the measured magnetisation for an increasing field is

$$M_\uparrow = \frac{J_c}{\pi R^2} \int_0^R (r - R)\, 2\pi r dr = -\frac{J_c R}{3}. \tag{2.36}$$

For a decreasing field we obtain

$$M_\downarrow = +\frac{J_c R}{3}. \tag{2.37}$$

Therefore the critical current density can be calculated from the measured width of the magnetic hysteresis loop per unit volume $\Delta M = |M_\downarrow - M_\uparrow|$ by the following equation

$$J_c = \frac{3\Delta M}{D} \tag{2.38}$$

where $D = 2R$ is the diameter of the cylinder. To obtain $J_c$ in its usual unit $A/cm^2$ from the measured $\Delta M$ in $emu/cm^3$ the modified formula

$$J_c \left( \frac{A}{cm^2} \right) = \frac{30\Delta M \left( \frac{emu}{cm^3} \right)}{D\,(cm)} \tag{2.39}$$

has to be used.

## 2.4 Sweep-rate dependence of the critical current

As reported by de Groot et al. [20] the width of a magnetic hysteresis loop depends on how quickly the magnetic field is swept when performing the measurement. Measuring the critical current density using magnetisation techniques is very common but the sweep-rate of the field $\beta = \frac{dH}{dt}$ is not usually reported in published papers.

Starting from equation 2.8 and 2.18 we obtain

$$\frac{J B a_0 \delta v}{k_B T} = \operatorname{arsinh} \left[ \frac{E}{2 a_0 \Omega_0 B} \exp \left( \frac{U_0}{k_B T} \right) \right] \tag{2.40}$$

and so at a given temperature and field this reduces to a scaling equation:

$$\frac{J}{J^*} = \text{arsinh}\left(\frac{E}{E^*}\right) \tag{2.41}$$

where

$$J^* = \frac{k_B T}{B a_0 \delta v} \tag{2.42}$$

$$E^* = \frac{2 a_0 \Omega_0 B}{\exp\left(\frac{U_0}{k_B T}\right)}. \tag{2.43}$$

As seen in equation 2.39 the critical current density is proportional to the width of the magnetic hysteresis loop per unit volume. Furthermore the electrical field is proportional to the change of the magnetic field by which it is generated $\left(E = 2\pi R \frac{dB}{dt}\right)$. So we can modify equation 2.41 to obtain a scaling equation describing the sweep-rate dependence of the critical current:

$$\frac{\Delta M}{\Delta M^*} = \text{arsinh}\left(\frac{\beta}{\beta^*}\right) \tag{2.44}$$

where

$$\Delta M^* = \frac{k_B T R}{15 B a_0 \delta v} \tag{2.45}$$

and

$$\beta^* = \frac{a_0 \Omega_0 B}{\pi R \exp\left(\frac{U_0}{k_B T}\right)}. \tag{2.46}$$

As mentioned before the continuity equation 2.9 can only be solved in the two limiting cases $\Delta W \gg k_B T$ and $\Delta W \ll k_B T$.

In the first case $\Delta W \gg k_B T$ the approximation $\sinh(x) = \frac{1}{2}\exp(x)$ for large $x$ made by Beasley et al. [4] (flux creep regime), leads to the scaling equation

$$\frac{\Delta M}{\Delta M^*} = \ln\left(\frac{2\beta}{\beta^*}\right). \tag{2.47}$$

In the latter (TAFF regime), discussed by Kes et al. [12], $E(J)$, which is equivalent to $\beta(\Delta M)$, was found to be linear (equation 2.21). Furthermore Fisher et al. [13, 14] predicted theoretically an $E(J)$- and therefore $\beta(\Delta M)$-dependence which follows a power-law (equation 2.26).

The investigation of the sweep-rate dependence of the width of the magnetic hysteresis loop can therefore deliver experimental information about the mechanism of flux motion.

## 2.5 Correlation between magnetic hysteresis and magnetic relaxation

In the previous paragraphs it was shown already that the magnetisation of a superconductor is related to its critical current (Bean) and that relaxation of the magnetisation with time results in a voltage (Maxwell and e.g. Beasley). In this paragraph these facts shall be used to derive a correlation between the sweep-rate dependence of the magnetisation and the relaxation of the magnetisation with time. In order to derive the scaling equation 2.44 describing the sweep-rate dependence of the critical current the proportionality between the width of a magnetic hysteresis loop and the current and also the proportionality between the electrical field and the sweep-rate were used as substitutions in equation 2.41. Now these substitutions shall be done in equation 2.19 which describes the electrical field due to flux motion according to the Anderson-Kim model. Doing so we obtain

$$2\pi R\beta = a_0\Omega_0 B \exp\left(-\frac{U_0}{k_B T}\left(1-\frac{\Delta M}{\Delta M_0}\right)\right) \tag{2.48}$$

where $\Delta M_0$ is related to the current density $J_{c_0}$ in the absence of any flux creep. Equation 2.48 can be rearranged in the form

$$\frac{\Delta M}{\Delta M_0} = \left[\frac{k_B T}{U_0}\ln\left(\frac{2\pi R}{a_0\Omega_0 B}\right)+1\right]+\frac{k_B T}{U_0}\ln\beta \tag{2.49}$$

or in an other form

$$\Delta M\,(\beta) = \Delta M_0\left(1-\frac{k_B T}{U_0}\ln\frac{\beta_0}{\beta}\right) \tag{2.50}$$

where

$$\beta_0 = \frac{a_0 \Omega_0 B}{2\pi R}. \tag{2.51}$$

This can again be rewritten as

$$\Delta M(\beta) = D_m + S \ln(\beta) \tag{2.52}$$

with the constant parameters

$$S = \Delta M_0 \frac{k_B T}{U_0} \tag{2.53}$$

and

$$D_m = \Delta M_0 - S \ln \beta_0. \tag{2.54}$$

A formula of similar form describing the relaxation of the magnetisation with time due to flux creep was derived by Beasley [4]:

$$\Delta M(t) = \Delta M_0 \left[1 - \frac{k_B T}{U_0} \ln\left(\frac{t}{t_0}\right)\right] \tag{2.55}$$

or rewritten

$$\Delta M(t) = \Delta M(1) - S \ln(t) \tag{2.56}$$

with the constant parameters

$$S = \Delta M_0 \frac{k_B T}{U_0} \tag{2.57}$$

and

$$\Delta M(1) = \Delta M_0 + S \ln(t_0). \tag{2.58}$$

The coefficient $S$ of $\ln(t)$ turns out to be the same as the coefficient $S$ of $\ln(\beta)$ in equation 2.52. Therefore the relation

$$\frac{\partial \Delta M}{\partial \ln(\beta)} = -\frac{\partial \Delta M}{\partial \ln(t)} \tag{2.59}$$

is valid following the assumptions of the Anderson-Kim and the Bean model.

The correlation between $\Delta M(t)$ and $\Delta M(\beta)$ was reported first by Pŭst et al. [21, 22, 23, 24]. This correlation seems to be quite promising in order to obtain more information with less experimental work and also gives the opportunity to prove how far the Anderson-Kim and the Bean model, on which it is based, can be used for the HTS-materials used in this work.

## 2.6 Temperature dependence of the critical current

Apart from the sweep-rate of the applied magnetic field and the value of the field itself the critical current also depends on the temperature. Tinkham [25] pointed out that $J_c$ should vary as a consequence of the Anderson-Kim model as

$$J_c \propto 1 - \alpha t - \beta t^2 \tag{2.60}$$

where $t = \frac{T}{T_c} \ll 1$ with the constant parameters $\alpha$ and $\beta$. Here the quadratic term is based largely on the temperature dependence of thermodynamic quantities, while the linear term can be determined by rearranging equation 2.20 :

$$J_c = \frac{U_0}{\delta v a_0 B}\left(1 - \frac{k_B T}{U_0}\ln\frac{a_0 B \Omega_0}{E_{min}}\right) \tag{2.61}$$

where $E_{min}$ is the electrical field criteria that defines $J_c$. If we substitute $t = \frac{T}{T_c}$ we obtain

$$J_c = \frac{U_0}{a_0 B \delta v}\left(1 - \alpha(B)\, t\right) \tag{2.62}$$

where

$$\alpha(B) = \frac{k_B T_c}{U_0}\ln\left(\frac{a_0 B \Omega_0}{E_{min}}\right) \tag{2.63}$$

Taking the temperature dependence of the thermodynamic quantities into account, $J_c(B,t)$ is given by

$$J_c(B,t) = \frac{U_0}{a_0 B \delta v}\left(1 - \alpha(B)\, t - \beta t^2\right). \tag{2.64}$$

To what extent this is valid will be investigated in chapter 5.

# Bibliography


[1] P. W. Anderson, Phys. Rev. Lett. **9**, 309 (1962)

[2] Y. B. Kim, C. F. Hempstead, and A. R. Strnad, Phys. Rev. Lett. **9**, 306 (1962)

[3] P. W. Anderson and Y. B. Kim, Rev. Mod. Phys., 39 (1964)

[4] C. P. Bean, Phys. Rev. Lett. **8**, 250 (1962)

[5] J. Bardeen, M. J. Stephen, Phys. Rev. **140**, 1197 (1965)

[6] P. W. Anderson in "Quantum Fluids" ed. D. F. Brewer (Amsterdam: North-Holland) on page 146

[7] M. R. Beasley, R. Labusch, and W. W. Webb, Phys.Rev. **181**, 682 (1969)

[8] C. W. Hagen, R. P. Griessen, and E. Salomons, Physica C **157**, 199 (1989)

[9] R. P. Griessen, J. G. Lensink, and B. Dam, Cryogenics **30**, 563 (1990)

[10] R. P. Griessen, Physica C **172**, 441 (1991)

[11] D. Dew-Hughes, Cryogenics **28**, 674 (1988)

[12] P. H. Kes, J. Aarts, J. van den Berg, C. J. van der Beek, and J. A. Mydosh, Supercond. Sci. Technol. **1**, 242 (1989)

[13] Matthew P. A. Fisher, Phys. Rev. Lett. **62**, 1415 (1989)

[14] Daniel S. Fisher, Matthew P. A. Fisher, Phys. Rev. B **43**, 130 (1991)

[15] M. V. Feigel'man, V. B. Geshkenbein, A. I. Larkin, and V. M. Vinokur, Phys. Rev. Lett. **63**, 2303 (1989)

[16] M. V. Feigel'man, V. M. Vinokur, Phys. Rev. B **41**, 8986 (1990)

[17] M. V. Feigel'man, Physica A **168**, 319 (1990)

[18] V. M. Vinokur, M. V. Feigel'man, V. B. Geshkenbein, and A. I. Larkin, Phys. Rev. Lett. **65**, 259 (1990)

[19] T. Nattermann, Phys. Rev. Lett. **64**, 2454 (1990)

[20] R. A. Rose, S. B. Ota, P. A. J. de Groot, and B. Jayaram, Physica C **170**,51 (1990)

[21] L. Půst, J. Kadlecová, M. Jirsa, and S. Durcŏk, J. low Temp. Phys. **78**, 179 (1990)

[22] L. Půst, M. Jirsa, J. Kadlecová, and S. Durcŏk, Cryogenics **30**, 886 (1990)

[23] L. Půst, Supercond. Sci. Technol. **3**, 598 (1990)

[24] M. Jirsa, L. Půst, J. Kadlecová, J. Magnetism and Magnetic Materials, **101**,105 (1991)

[25] M. Tinkham, Helvetica Physica Acta **61**, 443 (1988)

# Chapter 3

# Equipment

## 3.1 Introduction

In order to investigate superconducting properties, information about the magnetic behaviour of the superconductor as a function of an applied magnetic field, the rate with which the field is changed, the temperature and the time can be used. In this work a 12 Tesla Oxford-Instruments vibrating sample magnetometer (hereafter referred to as *VSM*) and various computing hard- and software equipment were used to obtain this information. Apart from the magnetisation, the grain-size of the sintered samples is necessary to determine the critical current density following Bean's model. As part of interdepartmental co-operation it was possible to use the scanning electron microscope (hereafter referred to as *SEM*) of the Geology Department to measure the diameter of the grains and compare the structure of the different samples.

## 3.2 The Vibrating Sample Magnetometer

Figure 3.1 shows a schematic sketch of the VSM, which works by moving the sample up and down between a set of pick-up coils with a frequency of $60Hz$ and an amplitude of $2mm$.

If the sample has a magnetic moment a voltage which is proportional to this is induced in the pick-up coils. The block diagram in figure 3.2 shows how the signal is produced. All instructions are fed in from the controlling

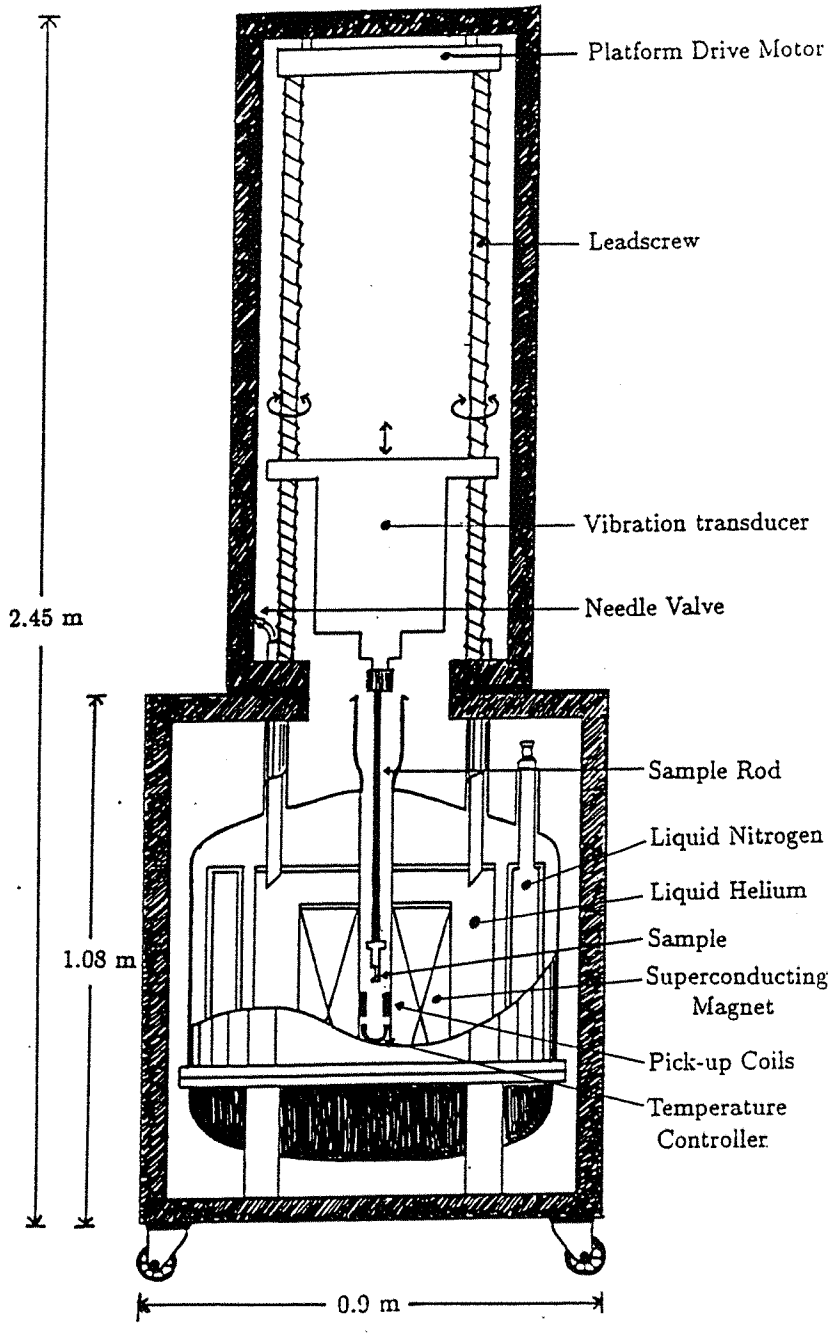


Figure 3.1: *Schematic sketch of the 12 Tesla Oxford-Instruments vibrating sample magnetometer.*

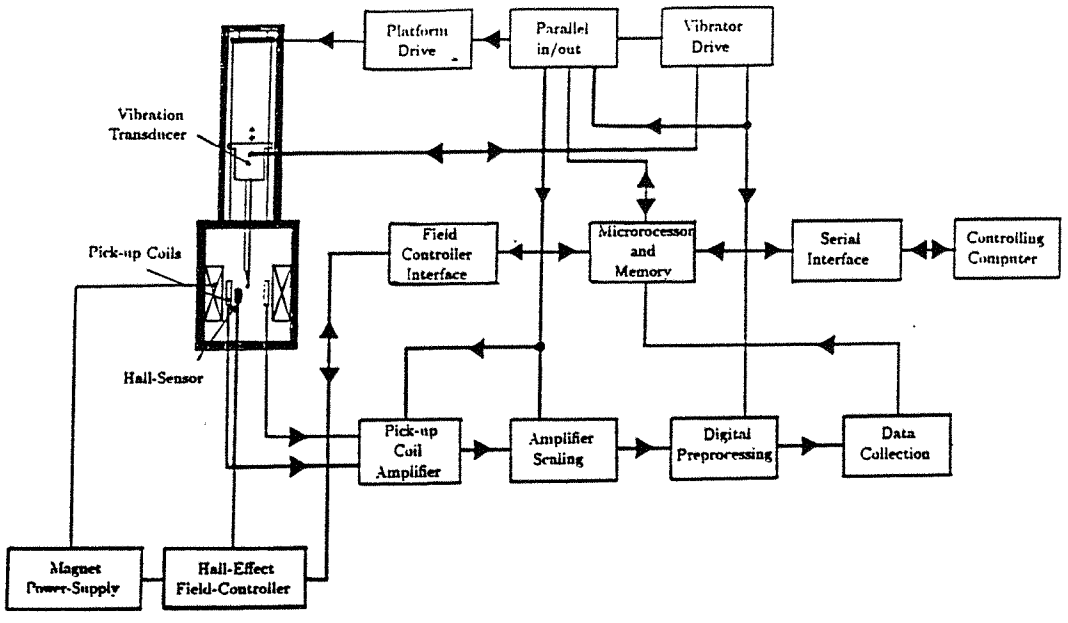


Figure 3.2: *Block diagram of VSM-data processing.*

computer at the start of the experiment. The unit then performs all the field control, data collection and storage operations as shown in figure 3.2.

The VSM consists of an Oxford 12 Tesla $NbTi/Nb_3Sn$ superconducting magnet in a long-hold cryostat with a useful helium volume of approximately 30 litres. The liquid helium has to be refilled every four days due to an average helium consumption of $300cm^3/h$. From the top of the cryostat a variable temperature insert (hereafter referred to as *VTI*) is loaded. Liquid helium is drawn from the main reservoir through a needle valve. This valve is adjusted from the top of the VTI and is used to control or stop the flow. From the needle valve the helium is piped to the sample space of the VTI. The heat exchanger is fitted with a gold-iron/chromel thermocouple for temperature measurement and a heater for temperature control.

For the range $4.2 - 100K$, temperature control is achieved by setting the flow-rate coarsely using the needle valve on the dewar. The temperature-controller (Oxford-ITC-4) gives fine control by regulating the power to the heater on the VTI heat exchanger.

Temperatures in the range $1.7-4.2K$ are obtained by reducing the vapour pressure of liquid helium after it has passed through the needle valve. In this

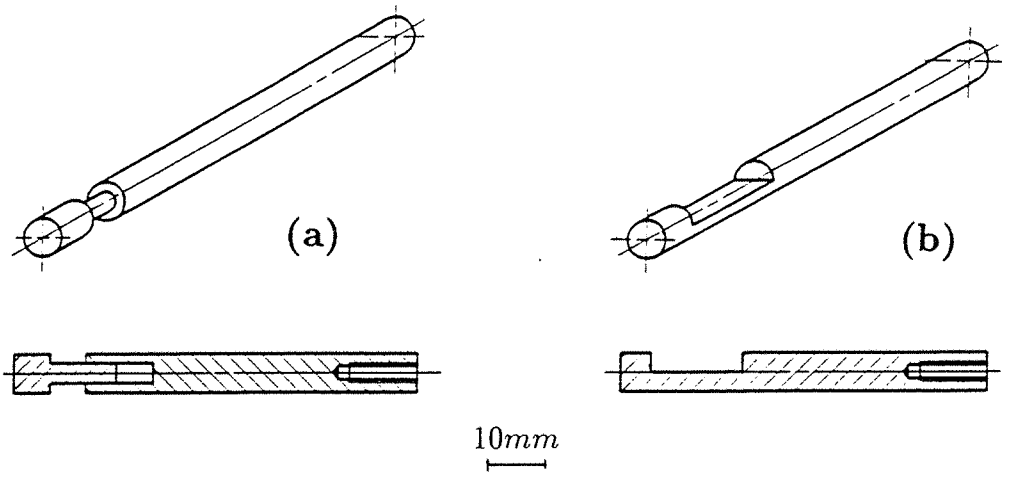


Figure 3.3: *(a) Powder sample holder; (b) Pressed-pellet sample holder.*

case, temperature control is achieved by the use of a pressure controller or manostat device to maintain the referral pressure over the liquid.

Between $100 - 300K$ the needle valve may be closed and the insert controlled at the set temperature by the electronics.

The remanent field of the magnet is approximately $5mT$. The field sweep-rate can be set between $0.01mT/s$ and $20mT/s$. It is possible to mount superconducting samples with a mass between $3mg$ and $3g$. They are placed on samplespecific sample holders which are screwed onto a carbon fibre rod. A sketch of the Tofnel sample holders used in this work is shown in figure 3.3. They were made in the students workshop with the assistance of Mr. Roszkewiak.

The software controlling the VSM was written by AEROSONIC. It allows measurements of the magnetisation versus the applied magnetic field, the temperature or the time. Unfortunately, due to software-restrictions, it was not possible to vary more than one parameter in $M(H,T,t)$ while a run was in progress or to change the sweep-rate of the applied magnetic field during an experiment. Before the start of a measurement the optimal sample position on the z-axis can be found by using a z-axis calibration routine. The software also gives the possibility to control the field and the temperature manually without performing a measurement. This is sometimes useful to obtain a well settled temperature before starting a measurement. Details on how the specific measurements were performed can be found in the following chapters where the experimental work is described.

## 3.3 Analysis software

At the end of an experiment the VSM-data is stored in the controlling-PC as a file consisting of just the measured magnetic moments, together with a header indicating the field, time or temperature interval between them and other measurement information. In order to analyse the data new programs were specially written by Tim Young and Richard Rose. They reconstruct the complete data sets from the stored information and convert them into ASCII-form suitable for importing into spreadsheets.

The built-in VSM-software assumes that the region of most interest in the data is near zero field. The field interval between data points is therefore ten times smaller between 0 and 1 Tesla than for 1 to 10 Tesla. Correspondingly the field intervals for data points between 10 and 12 Tesla are ten times larger than that in the 1 to 10 Tesla region. The translation software mentioned above averages output data with a regular field interval across the entire field range. In order to do calculations with the translated data these data-files were imported into *Quattro Pro 3.0.* The results of the calculations were then imported into the fitting program *TAS-fit.* This non-linear least-squares fitting program was written in *C* by Tim Young and Simon Smith. It uses the Levenberg-Marquardt Method to fit almost every mathematical function with up to five fitting-parameters to the measured data. The output can be displayed using *GLE*, a public domain graphics program which is compatible into LaTeX-text-files.

## 3.4 The Scanning Electron Microscope

The *Joel-JSM-6400* scanning electron microscope of the Geology Department is a high resolution one with a modern image processing system. The basic unit consists of an electron optical column mounted on the main console, a control and display system, a power supply unit and a pump box. A schematic diagram of it is shown in figure 3.5.

After the electron beam is focused on the specimen as indicated in figure 3.4, the secondary electrons emitted from the specimen are detected and converted into electronic signals by a secondary electron detector. This detector consists of a scintillator and a photomultiplier. The electrical signals are fed into a video amplifier. One channel of the video signal is displayed

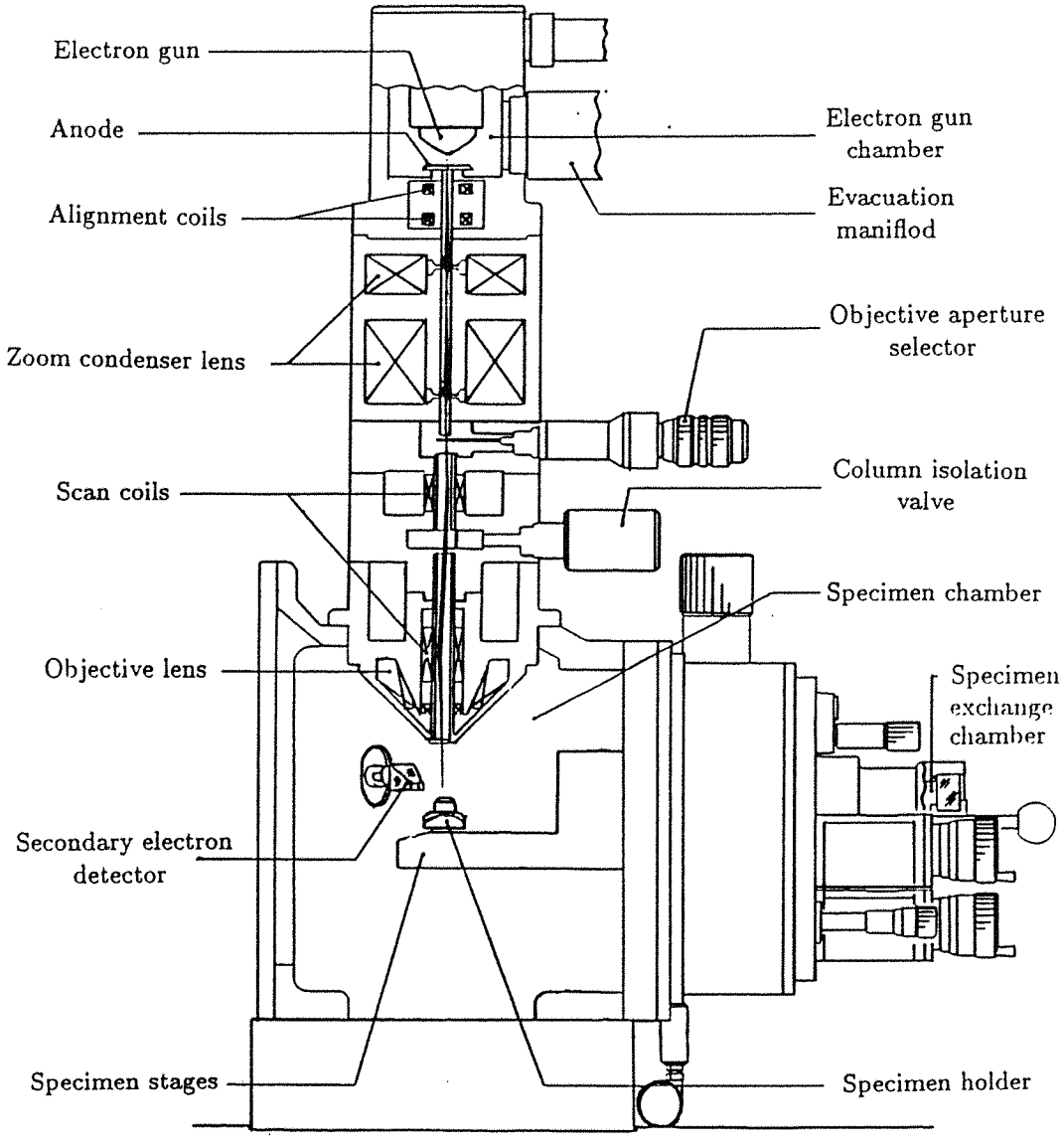


Figure 3.4: *Cross section of the column.*

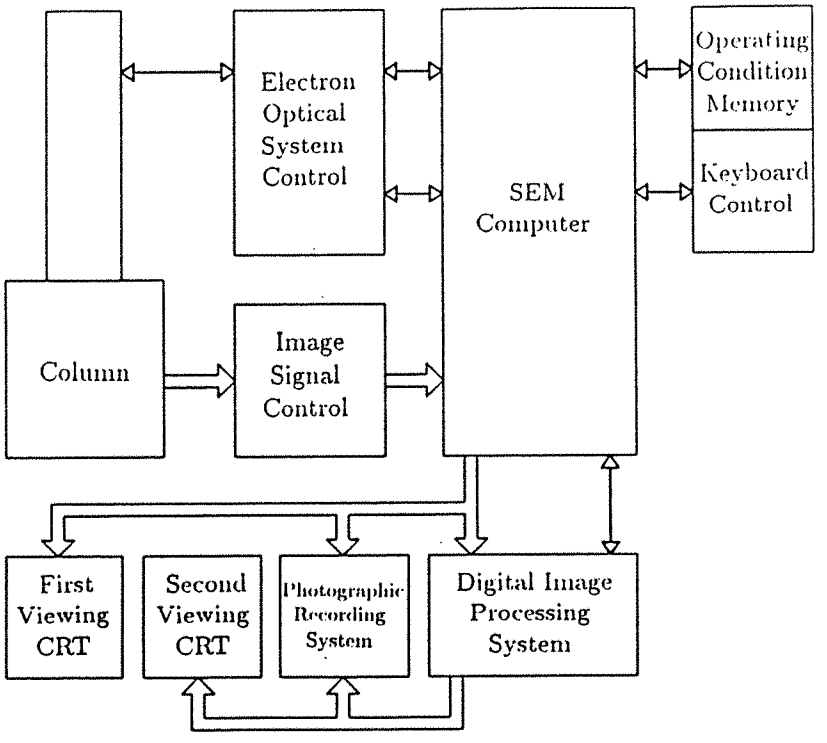


Figure 3.5: *Schematic diagram of the Joel-JSM-6400 scanning electron microscope.*

as a scanning image on the first viewing cathode ray tube (CRT). The other channel is digitized, recursively averaged to improve the signal to noise ratio and afterwards displayed as an image of high quality on the second viewing CRT. The image can be photographically recorded. The samples were fixed on the sample holder with conducting carbon cement. Thanks to the small size of the samples ($max.10 \times 5 \times 1mm$), three sample holders could be inserted into the specimen chamber at once. The specimen chamber is evacuated to an operating pressure of the order of $10^{-9}bar$. The range of movement of the sample in this chamber is $50 \times 70 \times 40mm$. The rotation range is not limited. Details about the image resolution, the acceleration voltage and the magnification are provided in the following chapters, where the results of the SEM measurements are shown.

# Chapter 4

# Comparative studies of differently prepared thallium-based superconductors

## 4.1 Introduction

It has always been tempting to try to relate the oxygen stoichiometry, structure and superconducting properties in high temperature superconductors but no systematic study of this has been made on the thallium cuprate superconductors so far. D. M. Ogborne prepared, as a part of the rolling grant collaboration, a large number of thallium-based superconducting samples which were investigated in this work. They were made in five separate series as shown in table 4.1.

The double thallium layer compounds are of particular interest because of their very high transition temperature. The series consist of samples with different oxygen contents obtained by different annealing processes. Resulting structural changes were discussed in the case of the powdered series in [1, 2]. In this chapter the resulting changes in terms of the superconducting properties of these materials will be discussed. This may hopefully be a contribution to find a reproducible way to prepare thallium-based superconductors with maximum critical current density and highest possible transi-

| $Tl_2Ba_2Ca_2Cu_3O_{10+\delta}$ ($\equiv$ Tl-2223) | |
|---|---|
| -first pressed pellet series | (6 samples) |
| -second pressed pellet series | (3 samples) |
| -powdered series | (3 samples) |
| $Tl_2Ba_2CaCu_2O_{8+\delta}$ ($\equiv$ Tl-2212) | |
| -pressed pellet series | (7 samples) |
| -powdered series | (3 samples) |

Table 4.1: *List of prepared series.*

tion temperature. Recently Liu et al.[3] reported a reproducible approach for attaining superconductivity at $128K$ in Tl-2223. Following their recipe, materials with apparently the same x-ray diffraction pattern were prepared here in Southampton. However, by looking at the neutron diffraction data [1] impurities were observed. This reveals one of the difficulties of the work on these materials: they are hard to reproduce ! This is due to the volatility of $Tl_2O_3$ and the narrow temperature range ($880 - 895^oC$) required to prepare single phase material. Another difficulty in working with these materials is the toxicity of thallium and its compounds. They have to be handled with extreme care. Contact of the metal with the skin is especially dangerous. Therefore safety-precautions such as wearing rubber gloves and a dust-mask must be taken.

## 4.2 Sample preparation

### 4.2.1 Solid state reactions

The way in which the solid state reactions were performed was basically the same for all the samples. First, single phase $BaCuO_2$ was synthesised by conventional solid state reaction from a stoichiometric mixture of $BaCO_3$ and $CuO$ at $900^oC$ for 48 hours in air. Then powders of $Tl_2O_3$, $BaCuO_2$, $CaO$ and $CuO$ were thoroughly ground in an agate mortar with nominal starting composition in the ratio of $Tl : Ba : Ca : Cu = 1.8 : 2 : 2.2 : 3$ as recommended for Tl-2223 by [4] and $Tl : Ba : Ca : Cu = 2 : 2 : 1 : 2$ in the case of Tl-2212. In some cases the reactant mixture (see table 4.2) was cold-pressed under $4kbar$ into pellets with diameter of $8mm$. The products were

| SAMPLENAME | POWDER | PELLET | QUENCHED | FURNACE | COOLED | NO ANNEALING | annealing parameters | | | |
|---|---|---|---|---|---|---|---|---|---|---|
| | | | | | | | GAS | PRESSURE | TEMPERATURE | TIME |
| Tl-2223/1pp/FC | | × | | × | × | | | | | |
| Tl-2223/1pp/AIR | | × | × | | × | | | | | |
| Tl-2223/1pp/OX | | × | × | | | | oxygen | $1atm$ | $500°C$ | $18h$ |
| Tl-2223/1pp/HPO | | × | × | | | | oxygen | $400atm$ | $500°C$ | $5h$ |
| Tl-2223/1pp/AR | | × | × | | | | argon | $1atm$ | $500°C$ | $18h$ |
| Tl-2223/1pp/FCP | × | | | × | × | | | | | |
| Tl-2223/2pp/AS | | × | | × | × | | | | | |
| Tl-2223/2pp/OX | | × | | × | | | oxygen | $1atm$ | $500°C$ | $18h$ |
| Tl-2223/2pp/AR | | × | | × | | | argon | $1atm$ | $500°C$ | $18h$ |
| Tl-2223/pow/AS | × | | | × | × | | | | | |
| Tl-2223/pow/HPO | × | | | × | | | oxygen | $500atm$ | $500°C$ | $5h$ |
| Tl-2223/pow/AR | × | | | × | | | argon | $1atm$ | $500°C$ | $12h$ |
| Tl-2212/pp/AS | | × | | × | × | | | | | |
| Tl-2212/pp/OXS | | × | | × | | | oxygen | $1atm$ | $500°C$ | $16h$ |
| Tl-2212/pp/OX | | × | | × | | | oxygen | $1atm$ | $500°C$ | $24h$ |
| Tl-2212/pp/HPO | | × | | × | | | oxygen | $500atm$ | $500°C$ | $18h$ |
| Tl-2212/pp/ARS | | × | | × | | | argon | $1atm$ | $500°C$ | $18h$ |
| Tl-2212/pp/AR | | × | | × | | | argon | $1atm$ | $500°C$ | $48h$ |
| Tl-2212/pp/ARL | | × | | × | | | argon | $1atm$ | $500°C$ | $88h$ |
| Tl-2212/pow/AS | × | | | × | × | | | | | |
| Tl-2212/pow/HPO | × | | | × | | | oxygen | $400atm$ | $500°C$ | $5h$ |
| Tl-2212/pow/AR | × | | | × | | | argon | $1atm$ | $500°C$ | $18h$ |

Table 4.2: *Preparation procedure of the investigated samples.*

sealed inside a gold tube to prevent loss of thallium at elevated temperatures and then calcined in a tube furnace under flowing oxygen at $890°C$ for 6 hours. Up to this point the preparation process was the same for all the samples, but the way in which the samples were afterwards cooled to room temperature differs.

Some samples were allowed to cool slowly to room temperature in four to six hours by just switching off the furnace, and some were cooled by taking them out of the furnace and quenching them in air. In this case it took just a few minutes to cool them down to room temperature.

### 4.2.2 Annealing process

The cold products of the solid state reaction were reground and split into equal quantities. The sample-specific further treatments of the solid state reaction products are shown in table 4.2. All annealing stages were followed by a slow cooling under the respective atmosphere. At these low annealing temperatures no weight reduction as a result of thallium loss from the sample was observed. The slow cooling was undertaken to ensure an even distribution of oxygen throughout the material. Quench cooling is likely to lead to an inhomogeneous oxygen ion distribution which would cause problems in determining the oxygen positional and occupancy parameters in the analysis of data from the diffraction experiments.

### 4.2.3 Sample characteristics

#### (a) General $Tl_2Ba_2Ca_{n-1}Cu_nO_{2n+4}$-structure

The structures of the homologous series $Tl_2Ba_2Ca_{n-1}Cu_nO_{2n+4}$ were elucidated by Subramanian et al.[5] who showed their close topological relationship to the bismuth structures. Structural modules with copper and alkaline earth cations are interleaved with $Tl_2O_2$ layers in the same sequence as in the $Bi$-phase. The thallium superconductors are close to the ideal tetragonal $I4/mmm$ symmetry at room temperature. These structures can be described with unit cells of approximately $3.9 \times 3.9 \times (17 + 6.2n)$ Å. The unit cell (shown in figure 4.1), in the case of Tl-2212, contains two and, in the case of Tl-2223, three $CuO_2$ layers which are separated by $Ca$ ions and two $TlO$ layers separated from each of the $CuO_2$ layers by a $BaO$ layer.

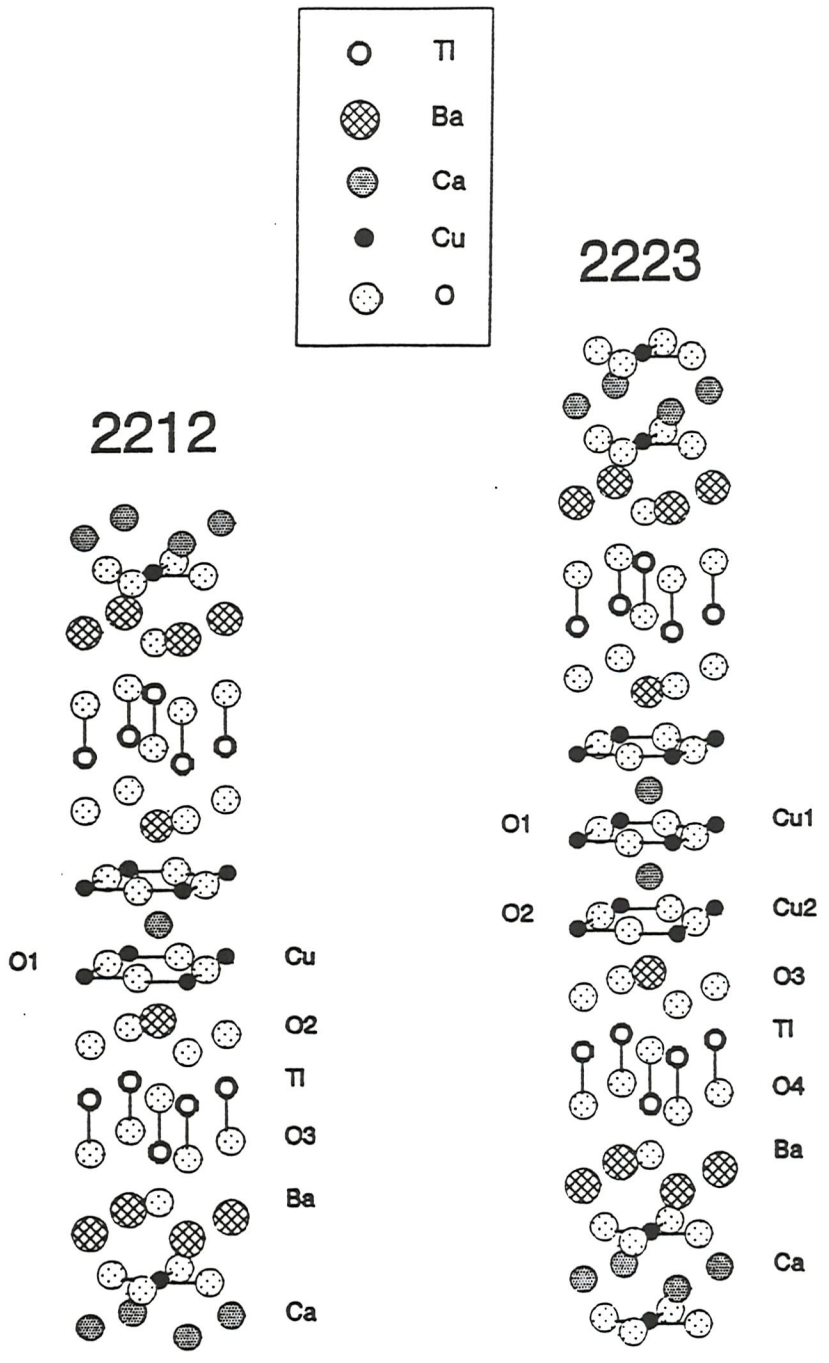


Figure 4.1: *Ball and stick representation of the Tl-2212 and the Tl-2223 structure.*

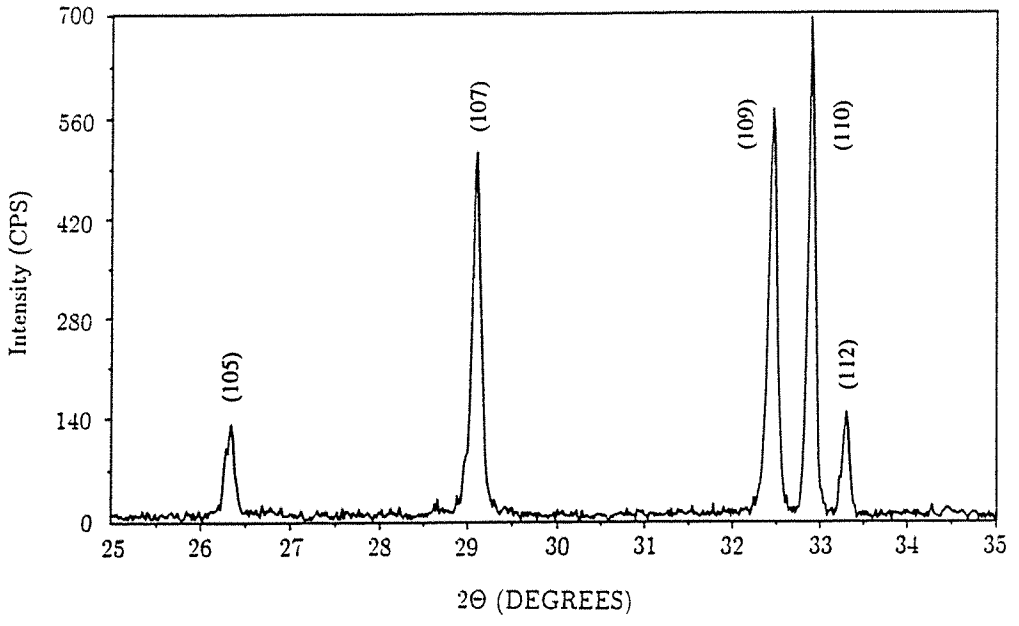


Figure 4.2: *PXD-pattern of Tl-2223/pow/AS.*

### (b) Powder x-ray diffraction

The samples were initially characterised by powder x-ray diffraction (PXD) in order to check sample purity and obtain unit cell parameters (table 4.3). Data was collected by D. M. Ogborne at room temperature over a range of 3° to 60° on a Siemens $D5000$ $\Theta - 2\Theta$ diffractometer using $CuK_{\alpha 1}$ radiation. As far as impurity is concerned, the $2\Theta$ range of interest is between 25° and 35°. Two characteristic PXD-patterns are shown in figure 4.2 and 4.3. Impurities occurring in Tl-2223 are most likely to be of the Tl-2212 phase and impurities in the Tl-2212 phase are usually $BaCuO_2$. They can be revealed in the PXD-pattern of the $25° - 35° 2\Theta$ range as peaks that can not be indexed to a Tl-2223 (or Tl-2212) phase. In the investigated samples almost all the peaks could be indexed to the corresponding phase.

Looking at the unit cell parameters, the analysis of the PXD data showed marked changes in the c-lattice parameter with annealing treatment. This effect can be illustrated by a shifting (109) peak while the (110) peak remains almost in the same position. This is shown in figure 4.4 for the case of the Tl-2212/pow-series.

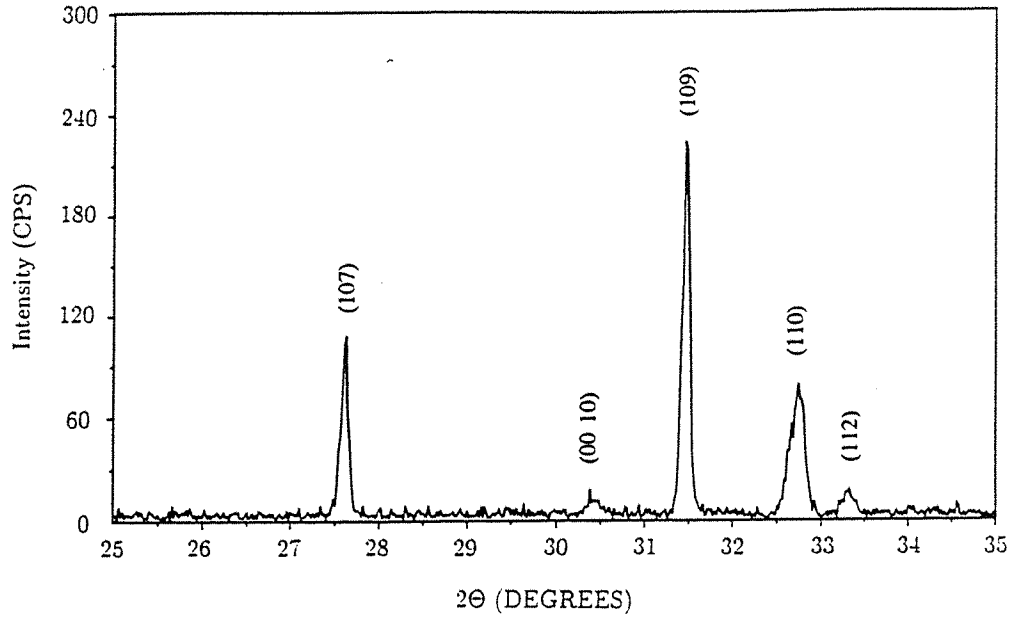


Figure 4.3: *PXD-pattern of Tl-2212/pp/AS.*

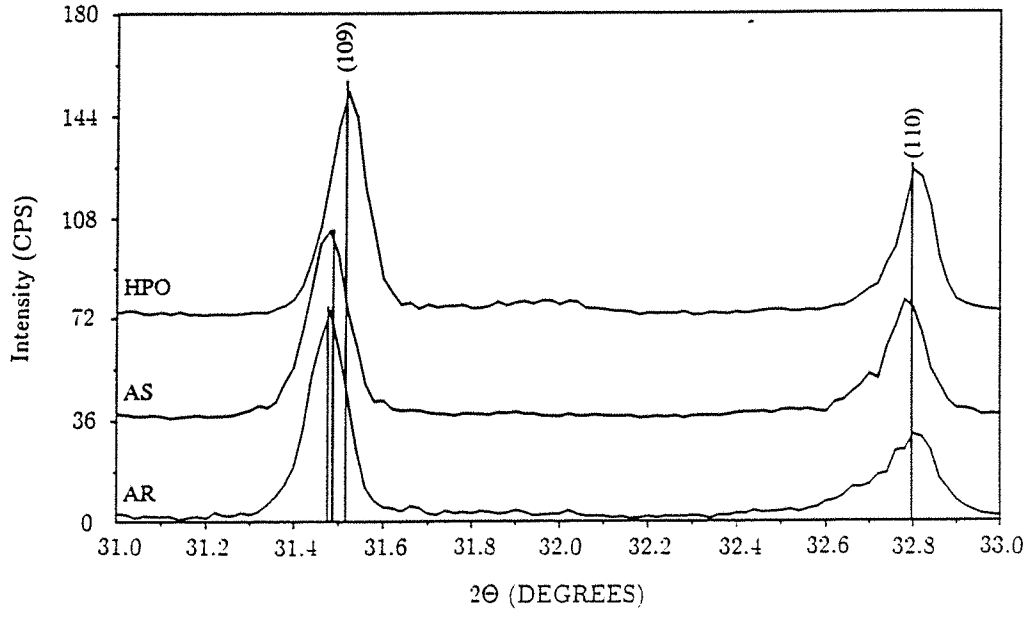


Figure 4.4: *Shifting* (109) *peak in the Tl-2212/pow-series.*

| samplename | a/Å | c/Å | samplename | a/Å | c/Å |
|---|---|---|---|---|---|
| Tl-2223/1pp/FC | 3.8508 | 35.6386 | Tl-2212/pp/AS | 3.8597 | 29.2779 |
| Tl-2223/1pp/AIR | 3.8511 | 35.6856 | Tl-2212/pp/OXS | 3.8637 | 29.3107 |
| Tl-2223/1pp/OX | 3.8542 | 35.6356 | Tl-2212/pp/OX | 3.8578 | 29.2967 |
| Tl-2223/1pp/HPO | 3.8541 | 35.6191 | Tl-2212/pp/HPO | 3.8612 | 29.2891 |
| Tl-2223/1pp/AR | 3.852 | 35.6554 | Tl-2212/pp/ARS | 3.8610 | 29.3322 |
| Tl-2223/1pp/FCP | 3.8508 | 35.6386 | Tl-2212/pp/AR | 3.8592 | 29.3271 |
| Tl-2223/2pp/AS | 3.8527 | 35.6288 | Tl-2212/pp/ARL | 3.8590 | 29.3290 |
| Tl-2223/2pp/OX | 3.8526 | 35.6329 | Tl-2212/pow/AS | 3.8594 | 29.321 |
| Tl-2223/2pp/AR | 3.8518 | 35.6691 | Tl-2212/pow/HPO | 3.8594 | 29.276 |
| Tl-2223/pow/AS | 3.8549 | 35.616 | Tl-2212/pow/AR | 3.8586 | 29.322 |
| Tl-2223/pow/HPO | 3.8591 | 35.612 | | | |
| Tl-2223/pow/AR | 3.8521 | 35.648 | | | |

Table 4.3: *Lattice parameters in Å as determined from PXD.*

### (c) Neutron diffraction

X-ray measurements are limited in determining oxygen positions and site occupancies in heavy metal oxides. In the case of the Tl-2223/pow- and Tl-2212/pow-series it was possible to collect neutron diffraction data at the Rutherford-Appleton Laboratory. Experimental details are described in [1, 2]. Inspection of the data show that the main change which occurs in the materials as a result of the various annealing treatments is in the occupancy of the oxygen site in the $TlO$ layer. This is shown in table 4.5. The variation in the lattice parameters as a result of the changes in the oxygen stoichiometry due to different annealing treatments is shown in table 4.4.

It can be seen that the a-parameter is almost invariant to changes in the oxygen stoichiometry, as guessed already from the x-ray data. The changes of the occupancy of the oxygen site in the $TlO$ layer are not reflected directly in the value of the c-dimension of these layers but rather in the $Cu-O$ apical bond distance shown in table 4.6.

The longer copper-oxygen apical bond length represents a lower hole concentration on the copper-oxygen planes due to a lower oxidation state of the copper-ion. This effects the superconducting properties as we shall see later in this chapter.

| | a/Å | c/Å |
|---|---|---|
| Tl-2223/pow/AS | 3.85101(1) | 35.58239(11) |
| Tl-2223/pow/HPO | 3.85167(1) | 35.56470(10) |
| Tl-2223/pow/AR | 3.85137(1) | 35.64292(11) |
| Tl-2212/pow/AS | 3.86049(1) | 29.33734(10) |
| Tl-2212/pow/HPO | 3.85972(1) | 29.29300(10) |
| Tl-2212/pow/AR | 3.86040(1) | 29.33717(10) |

Table 4.4: *Lattice parameters in Å as determined from neutron diffraction.*

| | Tl-2223/pow | Tl-2212/pow |
|---|---|---|
| AS | 6.4% vacant | 4.8% vacant |
| HPO | full | full |
| AR | 10.8% vacant | 6.4% vacant |

Table 4.5: *Occupancy of the oxygen-site in the TlO layer.*

| | Tl-2223/pow | Tl-2212/pow |
|---|---|---|
| HPO | 2.656(1) | 2.6103(4) |
| AS | 2.656(2) | 2.6480(4) |
| AR | 2.683(2) | 2.6574(5) |

Table 4.6: *$Cu-O$ apical bond distance in Å .*

| samplename | D/$\mu m$ | samplename | D/$\mu m$ |
|---|---|---|---|
| Tl-2223/1pp/FC | 20 | Tl-2212/pp/AS | 8 |
| Tl-2223/1pp/AIR | 15 | Tl-2212/pp/OXS | 8 |
| Tl-2223/1pp/OX | 15 | Tl-2212/pp/OX | 8 |
| Tl-2223/1pp/HPO | 15 | Tl-2212/pp/HPO | 8 |
| Tl-2223/1pp/AR | 15 | Tl-2212/pp/ARS | 8 |
| Tl-2223/1pp/FCP | 8 | Tl-2212/pp/AR | 8 |
| Tl-2223/2pp/AS | 11 | Tl-2212/pp/ARL | 8 |
| Tl-2223/2pp/OX | 11 | Tl-2212/pow/AS | 5 |
| Tl-2223/2pp/AR | 11 | Tl-2212/pow/HPO | 5 |
| Tl-2223/pow/AS | 8 | Tl-2212/pow/AR | 5 |
| Tl-2223/pow/HPO | 8 | | |
| Tl-2223/pow/AR | 8 | | |

Table 4.7: *Average grain-size (diameter in $\mu m$).*

### (d) Scanning electron microscopy

Beside the structure parameters of the material the size of the grains is an important quantity of the sample. In order to determine the diameter of the grains, which is necessary to calculate the critical current density of the sample, measurements were done with the scanning electron microscope described in the previous chapter. The chosen acceleration voltage of the electron gun was $20KV$. Magnifications between $1000\times$ and $5000\times$ were used to get an impression of the order of grain sizes and of the detailed shape of the grains themselves. Examples of the photographs taken are shown in figure 4.5.

The average grain-size was determined by taking the average over 50 grains shown on the photographs. The values are given in table 4.7.

The different grain-sizes in one series are due to separate grinding procedures after the solid state reaction.

(a)

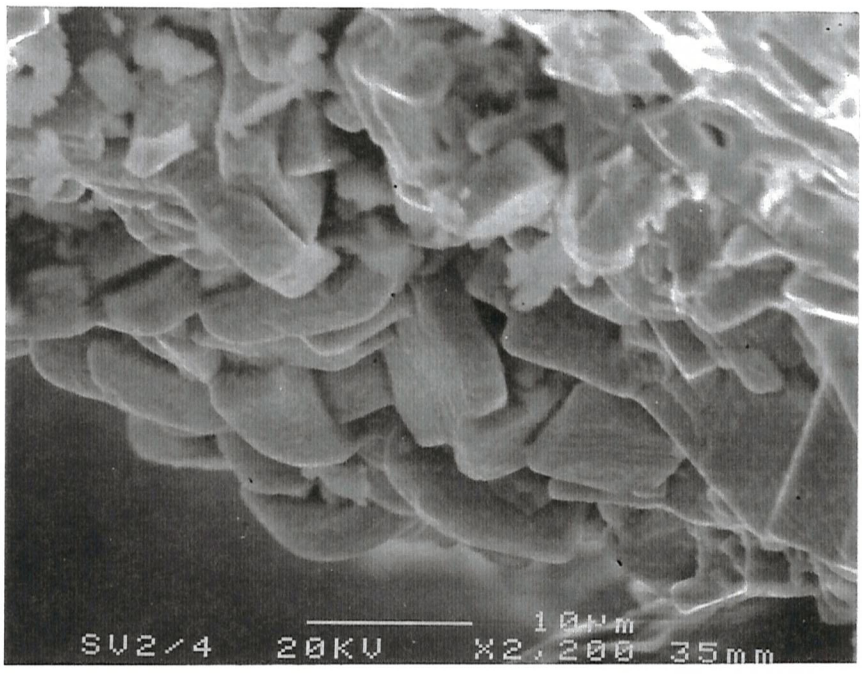


(b)

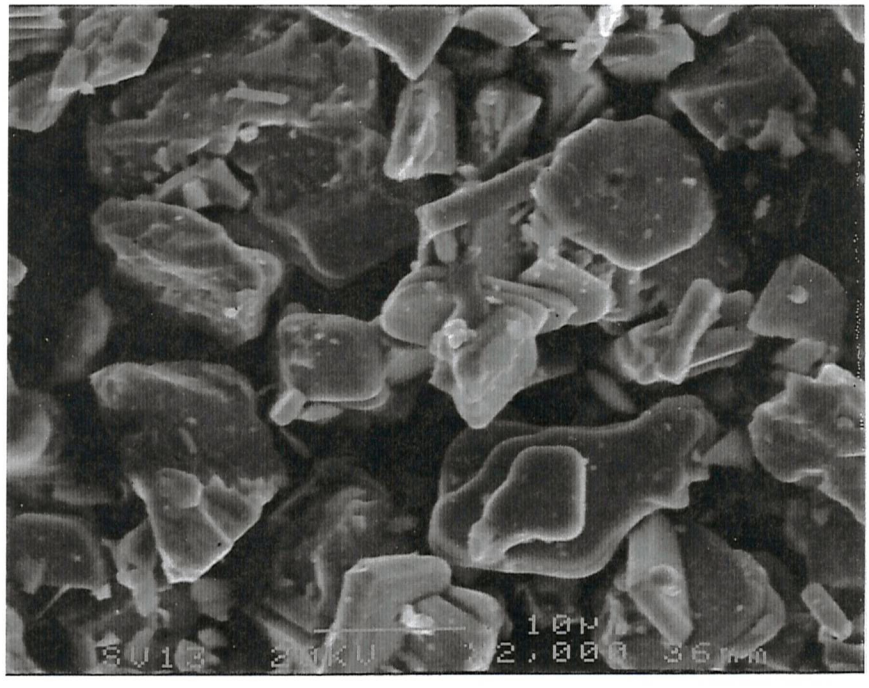

Figure 4.5: *Photographs of (a) the edge of the Tl-2212/pp/OX sample and (b) the Tl-2223/pow/HPO sample taken with the SEM.*

## 4.3 Superconducting properties

### 4.3.1 The transition temperature

The transition from the superconducting state into the normal state is characterised by the complete loss of the diamagnetic behaviour of the sample at the transition temperature $T_c$. This effect was used to determine $T_c$ values with the VSM. The sample was cooled at zero field from above $T_c$ down to $10K$. A field of $10mT$ was applied and the temperature was swept up to $150K$ in steps of $0.2K$ with a settle time of $5s$ at each point. These are the optimal parameters for performing a temperature sweep in order to make sure that the measured temperature is really the sample temperature as found by comparing the shown temperature of the ITC4 temperature controller with the real sample temperature using the ordering transitions of $NiCl_2$, $KMnF_3$ and $KCoF_3$. Due to the time constants of the system, the shown temperature during a temperature decrease is always smaller than the real temperature whereas these values correspond much better in the case of increasing temperature. For this latter case the above chosen parameters gave the best correspondence. In figure 4.6 the magnetisation decreases and disappears at a transition temperature of $121K$. The measured $T_c$ values for all samples are shown in table 4.8.

As one can see from the Tl-2223/1pp-series, which was the first prepared series, furnace cooling leads to a much higher $T_c$ than quenching in air. Therefore all the samples of the following series were allowed to cool slowly in the furnace. The next step to improve the $T_c$ value was done by using the different annealing procedures described above.

In the case of the Tl-2223/pow- and Tl-2212/pow-series the neutron data provided information about the copper-oxygen apical bond distances which is controlled by the oxygen stoichiometry as seen in table 4.6. This $Cu-O$ bond distance appears to be the most influential parameter in regulating the average oxidation state of the copper atoms, and hence the hole concentration, which in turn determines the superconducting properties of the material. In general the copper-oxygen apical bond distances calculated for the Tl-2223 materials were greater than those for the Tl-2212 compounds leading to lower average $Cu$ valence. However, it was noted that the bond distances of the highest $T_c$ samples (Tl-2223/pow/AS and Tl-2212/pow/AR) were of approximately of the same value, 2.656 Å and 2.657 Å respectively.

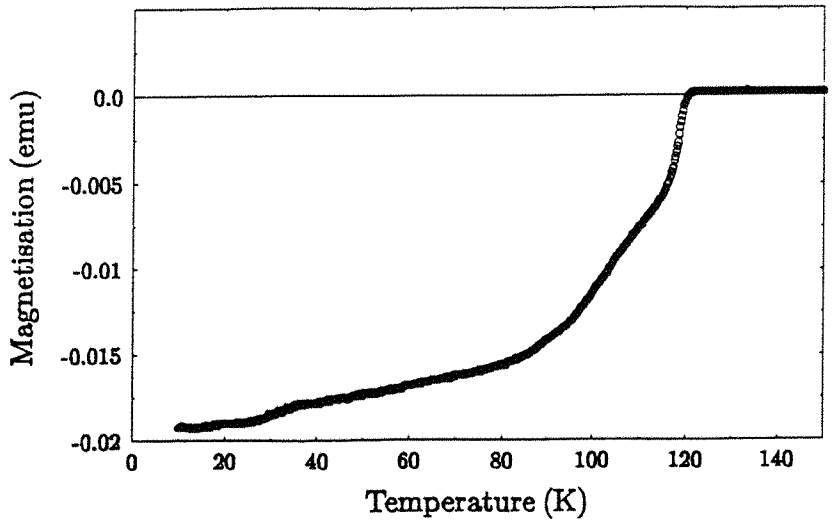


Figure 4.6: *Transition temperature measurement of Tl-2223/1pp/FCP with the VSM.*

| samplename | $T_c/K$ | samplename | $T_c/K$ |
|---|---|---|---|
| Tl-2223/1pp/FC | 121 | Tl-2212/pp/AS | 103 |
| Tl-2223/1pp/AIR | 106 | Tl-2212/pp/OXS | 103 |
| Tl-2223/1pp/OX | 107 | Tl-2212/pp/OX | 105 |
| Tl-2223/1pp/HPO | 113 | Tl-2212/pp/HPO | 103 |
| Tl-2223/1pp/AR | 106 | Tl-2212/pp/ARS | 103 |
| Tl-2223/1pp/FCP | 121 | Tl-2212/pp/AR | 102 |
| Tl-2223/2pp/AS | 111 | Tl-2212/pp/ARL | 101 |
| Tl-2223/2pp/OX | 109 | Tl-2212/pow/AS | 106 |
| Tl-2223/2pp/AR | 103 | Tl-2212/pow/HPO | 101 |
| Tl-2223/pow/AS | 117 | Tl-2212/pow/AR | 107 |
| Tl-2223/pow/HPO | 115 | | |
| Tl-2223/pow/AR | 109 | | |

Table 4.8: *Transition temperatures as determined with the VSM.*

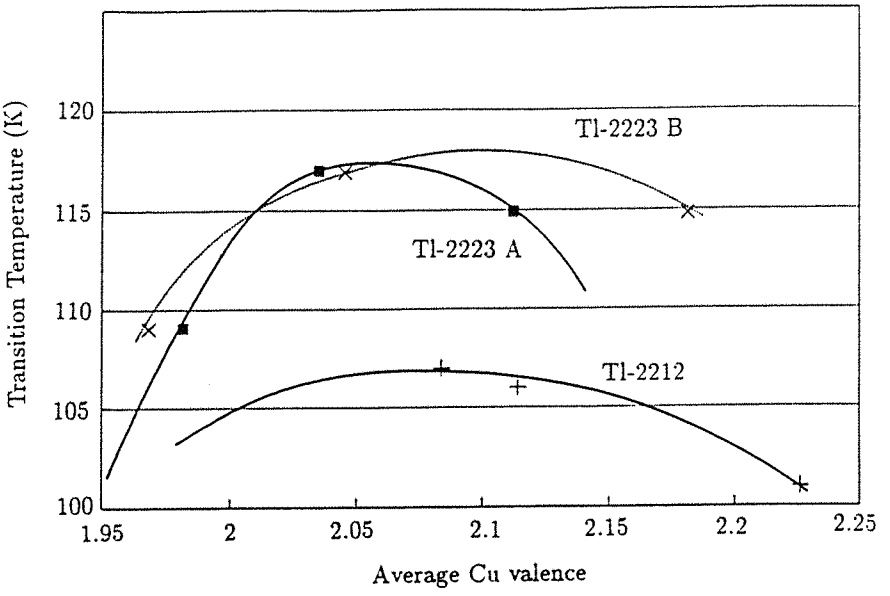


Figure 4.7: *Transition temperatures of the Tl-2212/pow and Tl-2223/pow series as a function of the average Cu oxidation state.*

Careful inspection of the other bond distances also reveals that the equatorial $Cu - O$ bonds are slightly longer in the Tl-2212/pow-series which may act to reduce the effective Cu valence. The $Cu - O$ interlayer separations are also significantly larger. Figure 4.7 shows the behaviour of the superconducting transition temperature with respect to the average $Cu$ oxidation state for the Tl-2212/pow- and Tl-2223/pow-series assuming all $Tl(III)$. If in Tl-2223/pow the valence of the copper atoms in the square planar coordination is taken as $Cu(II)$ only, the calculated valence of the copper atoms in the square pyramidal units increases relative to the case where some $Cu(III)$ is assumed to occur on the square planar site. This is shown in the dotted curve which more closely resembles the curve for Tl-2212/pow indicating that the valence of the coppers in the pyramid are very similar for both compounds.

The annealing treatment which leads to the improvement of the $T_c$-value is strongly dependent on the oxygen stoichiometry of the *as prepared* sample and also to some extent on the number of CuO planes, as will be shown later. In the case of the Tl-2223/pow-series, reduction in the oxygen stoichiometry in the thallium-oxygen planes, as a result of argon annealing, is reflected in a lowering of the critical temperature. High pressure oxygen annealing

increases the oxygen stoichiometry but does not improve the transition temperature, probably indicating that the maximum in the $T_c$ vs hole concentration plot has been reached. In the Tl-2212/pow-series, argon annealing has been found not to lower $T_c$ but high pressure oxygen annealing led to a decrease in the transition temperature which is due to another position of the *as prepared* sample hole concentration on the $T_c$ vs hole concentration curve.

These curves explain the effects of variations in $T_c$ with the oxygen content and fit broadly with the behaviour modelled [6]. Plots like figure 4.7 cannot be drawn for the other series which were not analysed by neutron measurements because information about the exact values of the oxygen stoichiometry or copper valence are lacking. But, as can be seen from the values of table 4.8, the trend of the transition temperature change due to different annealing procedures is consistent with the behaviour shown in figure 4.7.

### 4.3.2 The critical current density

In chapter 2 it was shown that the critical current density $J_c$ of a superconductor can be calculated from a magnetic hysteresis loop. As mentioned in chapter 3, a 12 Tesla Oxford-Instruments vibrating sample magnetometer was used in this work to measure the magnetic hysteresis of the investigated samples. The experiments were performed as follows:

After placing the sample in the optimal position between the pick-up coils, determined by the z-axis test, it was cooled down in zero field from at least $150K$ to the operation temperature of the measurement. The measurements to investigate the critical current density of differently prepared samples were all performed at $4.2K$ and $30K$. To make sure that the temperature was really stable during the whole measurement, it was settled at the required value for about 10 minutes before the magnetic field was applied. Knowing that the critical current density is dependent on the sweep-rate with which the magnetic field is applied, as seen in chapter 2, the magnetic field was changed in all experiments of this chapter with the value of $20mT/s$. It was swept up to 6 Tesla, down to -2 Tesla and up again to +2 Tesla. The field went automatically back to zero after each measurement. Therefore it was always necessary to warm the sample up to a temperature above $T_c$ before starting the next experiment in order to avoid any remanence trapped in the sample. Figure 4.8 shows an example of the measured hysteresis loops.

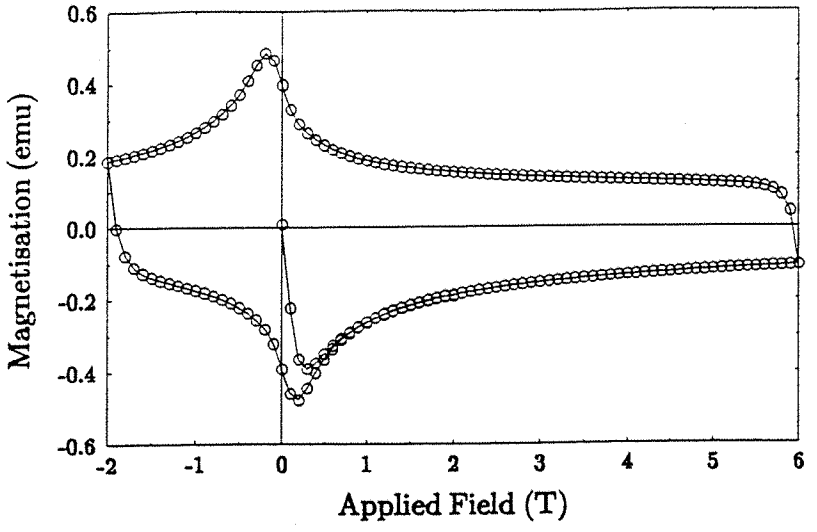


Figure 4.8: *Magnetic hysteresis loop measured with the VSM at* $4.2K$ *with a sweep-rate of* $20mT/s$ *on Tl-2212/pow/HPO.*

The shape of the curve is the result of the superposition of the equilibrium magnetisation for a type II superconductor and the irreversible hysteresis of a fully penetrated sample as assumed in the Bean model in chapter 2. The width of these hysteresis loops $\Delta M = |M_{\downarrow} - M_{\uparrow}|$ was divided by the volume of the sample, which was obtained from their mass, the mass of one unit cell according to the composition of the solid state reaction and the volume of the unit cell determined from the cell-parameters measured in XRD and neutron diffraction. Further dividing by the grain-size gives the critical current density as already shown in equation 2.39:

$$J_c\left(\frac{A}{cm^2}\right) = \frac{30\Delta M\left(\frac{emu}{cm^3}\right)}{D\,(cm)}$$

The results of $J_c$ as a function of the applied field are shown in figures 4.9 to 4.14 for all five measured series.

The shape of these graphs will be discussed in the next chapter. In this part of the work attention is only drawn to the comparison of the values of the critical current density at fixed temperature and field. In figure 4.9 it can be seen that furnace cooling leads to a much higher critical current density

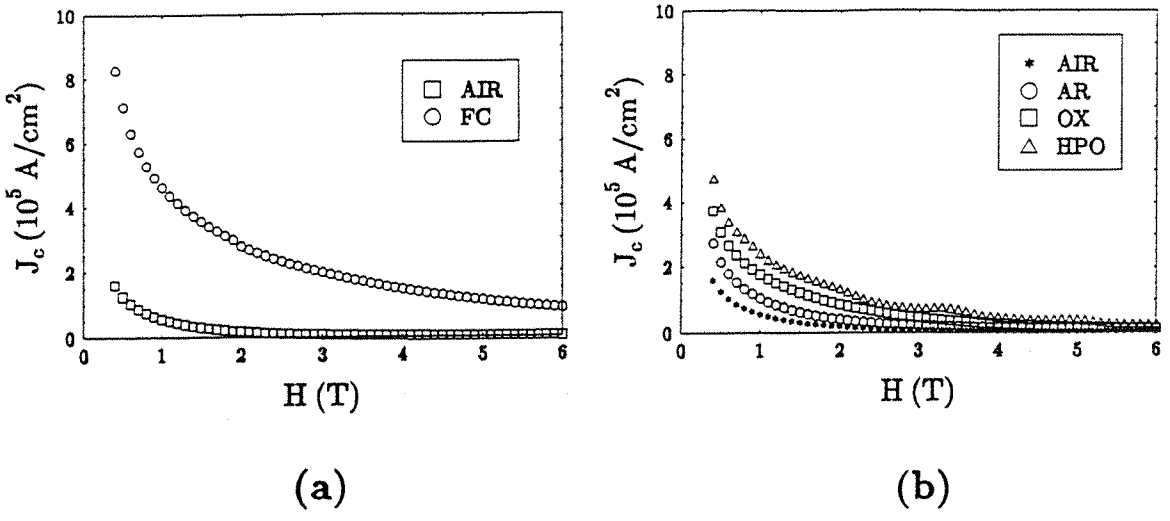


Figure 4.9: *Critical current density plotted versus the applied magnetic field at 30K for (a) Tl-2223/1pp/AIR and FC, (b) Tl-2223/1pp/AIR, AR ,OX and HPO.*

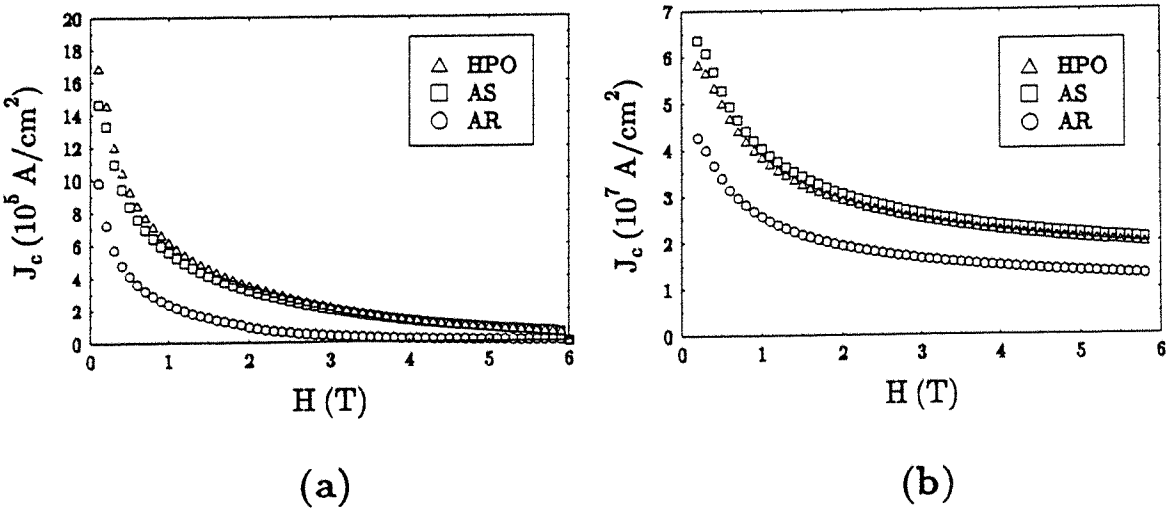


Figure 4.10: *Critical current density plotted versus the applied magnetic field for Tl-2223/pow/AR, AS and HPO at (a) 30K and (b) 4.2K.*

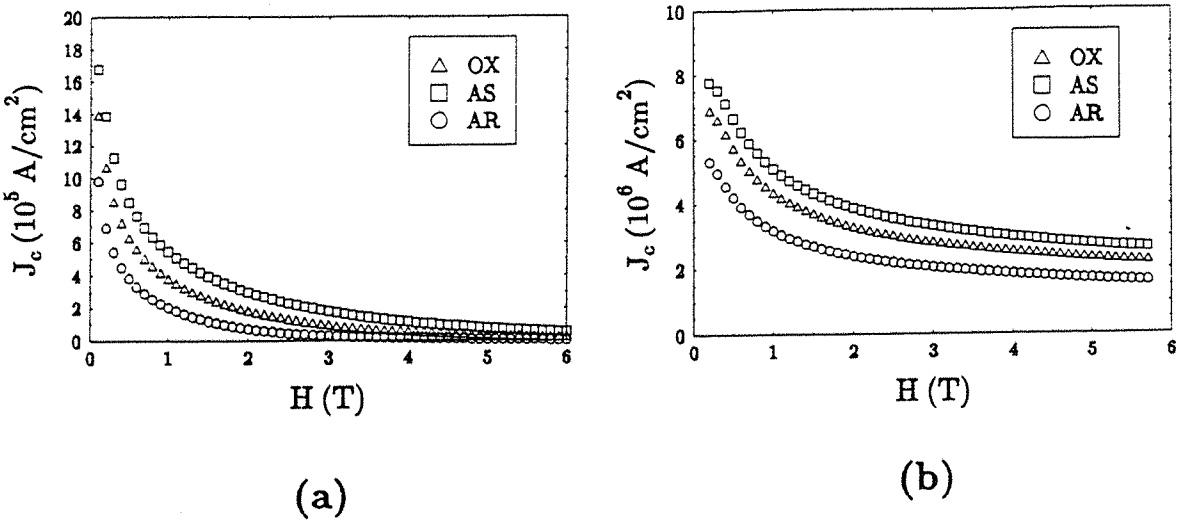


Figure 4.11: *Critical current density plotted versus the applied magnetic field for Tl-2223/2pp/AR, AS and HPO at (a) 30K and (b) 4.2K.*

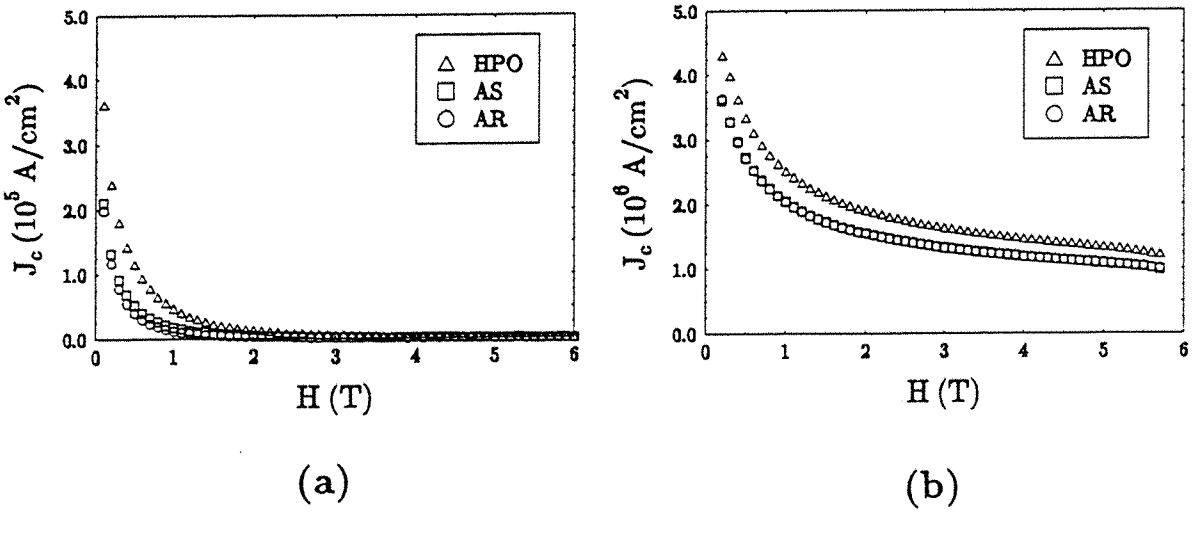


Figure 4.12: *Critical current density plotted versus the applied magnetic field for Tl-2212/pow/AR, AS and HPO at (a) 30K and (b) 4.2K.*

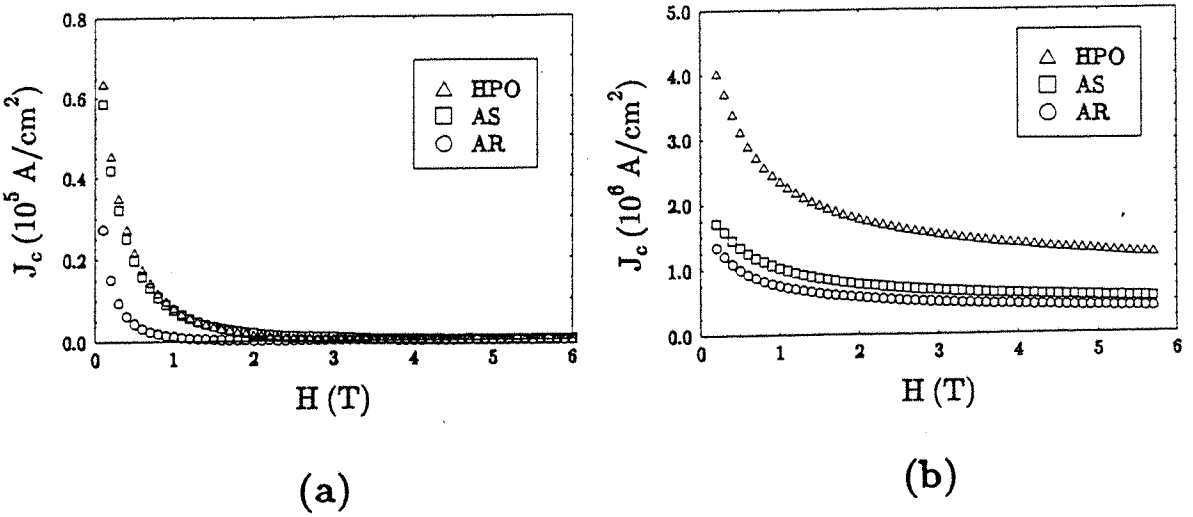


Figure 4.13: *Critical current density plotted versus the applied magnetic field for Tl-2212/pp/AR, AS and HPO at (a) 30K and (b) 4.2K.*

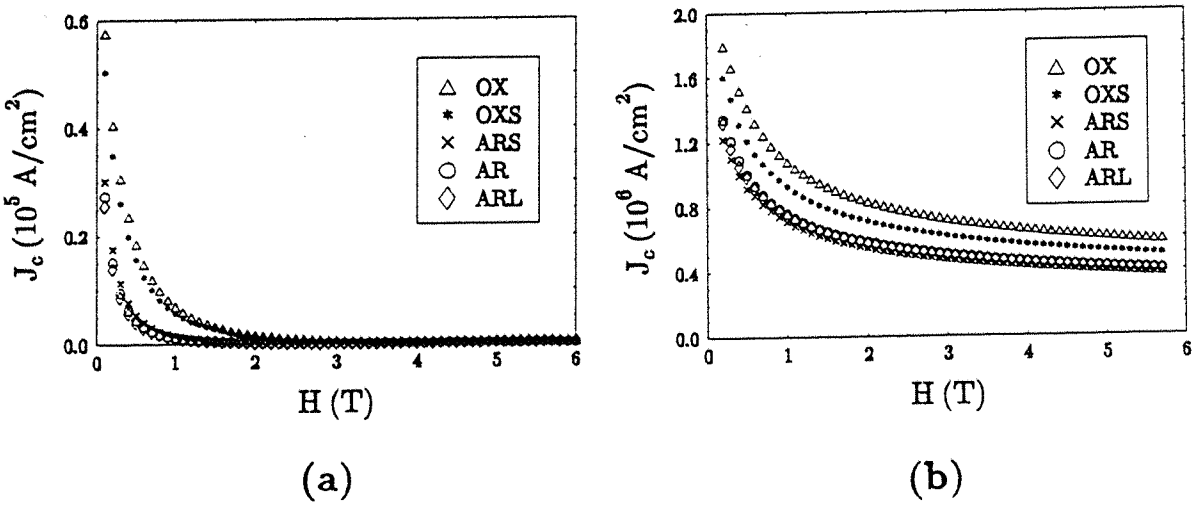


Figure 4.14: *Critical current density plotted versus the applied magnetic field for Tl-2212/pp/ARL, AR, ARS, OXS, OX and HPO at (a) 30K and (b) 4.2K.*

than quenching in air. This is consistent with the behaviour observed for the transition temperature as shown in the previous section. The reason for this drastic improvement of the quality of the superconducting properties resulting from slow cooling is that the ions are much more accurately located in their proper positions after slow cooling than after quenching in air. Especially the oxygen-ions show a more random rather than ordered distribution in the quenched samples. Based on these results of the first prepared series it was decided to cool all further prepared samples slowly in the furnace. However, in the series of the quenched samples itself (figure 4.9(b)) it can be seen that further annealing generally leads to an improvement of the critical current density. This results from the reordering of the ions during the annealing process and the following slow cooling. It is again consistent with the values obtained for the transition temperature as shown in table 4.8. Furthermore this first series reveals already what can be found in *all* following series by looking at figures 4.9 to 4.14: The critical current density increases as the oxygen concentration of the annealing gas is raised !

In particular the argon annealed samples have in all the series lower values of the critical current density than the samples which were annealed with oxygen. The duration of the annealing procedure and the pressure of the annealing gas are found to be of importance as well. Even if the resulting changes of the $J_c$ values are small, as can be seen in figure 4.14, they are consistent in themselves and confirm the general trend that the critical current density increases with the intensity of oxygen annealing and decreases with the intensity of argon annealing.

A systematic study like this has never been done before on thallium-based superconductors. The only other group, which reported at least an attempt to increase the transition temperature by changing the hole concentration with post-annealing techniques, was very recently the group of T. Kaneko et al. [7]. However, apart from the fact that the hole concentration on the copper-oxygen planes and the Tl-content is of importance, no explanation for the changing superconducting properties due to different annealing procedures has been reported so far.

In this work a consistent trend of an increase of the critical current density with an increasing hole concentration has been observed. This can be seen by comparing the results of the neutron scattering experiments on the Tl-2223/pow and Tl-2212/pow series with the measured critical current density values. In both series it has been observed that the $Cu-O$ apical bond

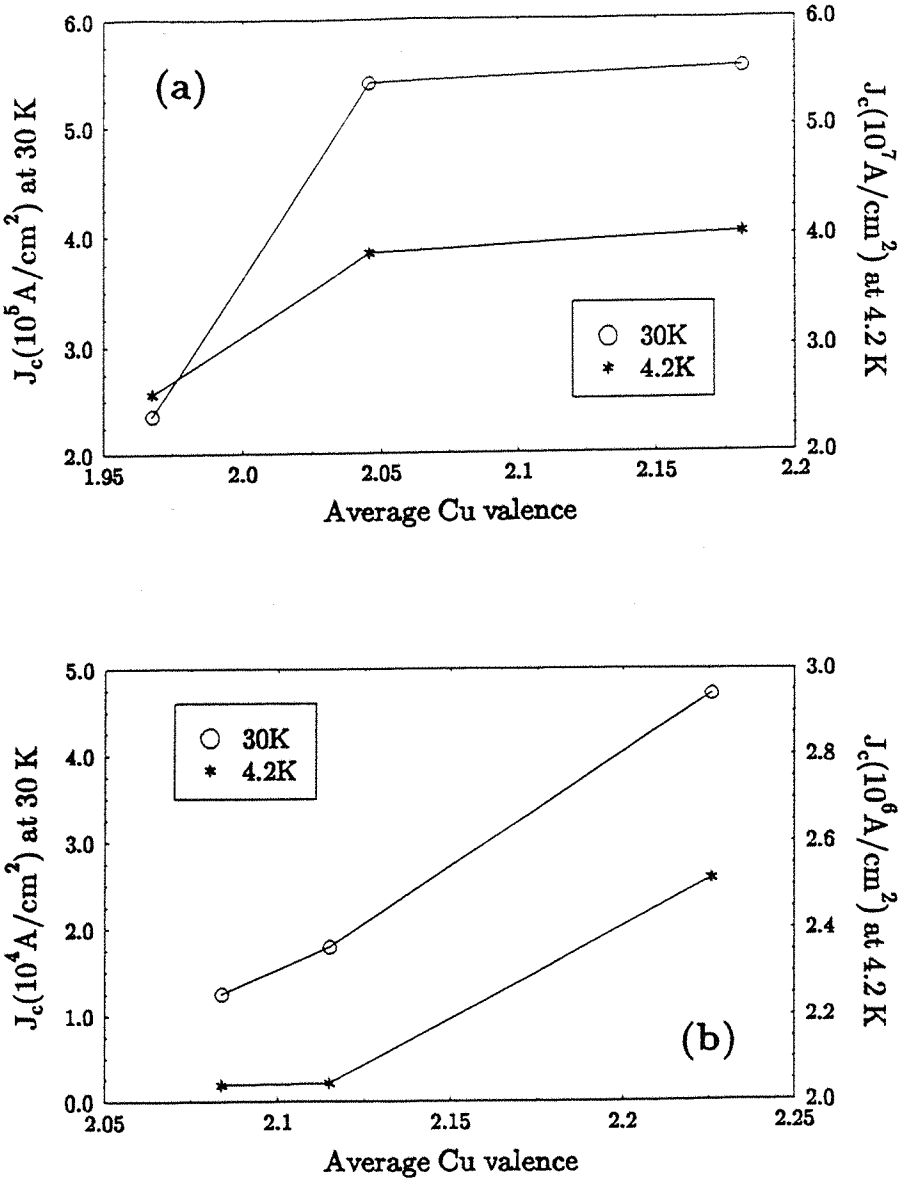


Figure 4.15: *Plot of the critical current density versus the average copper valence for (a) Tl-2223/pow and (b) Tl-2212/pow.*

length is much longer in the argon annealed samples than it is in the oxygen annealed ones (table 4.6). The longer copper-oxygen apical bond length represents a lower hole concentration on the copper-oxygen planes due to a lower oxidation state of the copper ion. Plots of the critical current density versus the average copper valence for both series are shown in figure 4.15 for different temperatures at 1T.

They show the increase of $J_c$ with an increasing average Cu valence which is a measure of the hole concentration on the copper-oxygen planes. However, several aspects have to be considered in an interpretation of this so far unknown systematic dependence of the critical current density on the annealing procedure:

First an attempt was made to find a connection between the hole concentration on the copper-oxygen planes and the vortex motion. R. A. Rose observed [8] that a higher hole concentration on the copper-oxygen planes is connected with a smaller penetration depth. This has been proved in [8] by Muon-Spin Rotation experiments. Unfortunately they were not possible in this work. At this point it is assumed that this relation is valid here as well. The penetration depth affects the interaction between the vortices, as it is shown for example by Tinkham [9]. Simulations of vortex systems with different values of the penetration depth have been made here in Southampton by D. J. Newman. Here the vortices and the pinning centres have been described using the assumptions that the pinning centres are all of equal strength, and that the density of pinning centres is less than the vortex density. Furthermore the vortices were all assumed to move independently. The number of pinning centres has been kept constant in a series. The results of the simulations show a larger movement of the vortices as the penetration depth decreases. This is also supported by the results of Larkin and Ovchinnikov [10] who found in their theory of collective pinning

$$F_p = BJ_c = \frac{n^2 f^4}{16 a_0^3 C_{44} C_{66}^2}$$

where n is the density of pinning centres, f is the force of interaction of an individual pinning centre with the lattice and $C_{66}$ and $C_{44}$ are elastic moduli of the flux line lattice. All this indicates that some of the assumptions made above do not correspond to the true nature of the pinning mechanism. Recent calculations of D. J. Newman, based on the quasi-spin model of superconductivity [11], indicate that the penetration depth does not necessarily decrease

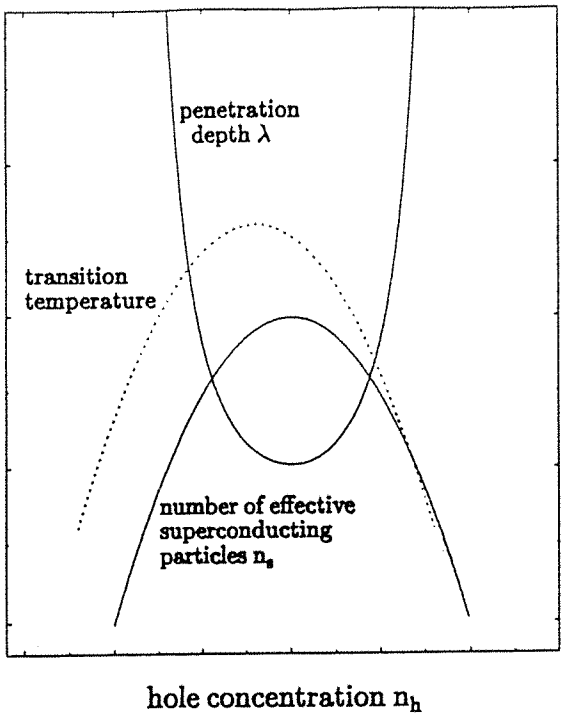


Figure 4.16: *Dependence of the number of effective superconducting particles* $(n_s)$ *and the penetration depth* $\lambda$ *on the hole concentration* $(n_h)$).

with an increasing hole concentration on the copper-oxygen planes, as assumed above following the results of the Muon-spin rotation experiments on doped $Bi_2Sr_2(Ca_{1-x}R_x)Cu_2O_{8+\delta}$, where R is a rare-earth dopant. The calculations show actually an inverse parabolic dependence of the number of effective superconducting particles $(n_s)$ on the hole concentration $(n_h)$, as illustrated in figure 4.16.

The number of superconducting particles is related to the penetration depth via

$$\lambda^2 = \frac{m}{e^2 n_s \mu_0}$$

as can be derived from the London-Equations. Figure 4.16 shows that the penetration depth does therefore not necessarily decrease with an increasing

hole concentration. The behaviour is very much dependent on the range of the hole concentration in the specific samples. Earlier quasi-spin calculations [6, 12] have shown that the maximum of the $n_s$ versus $n_h$ plot occurs at almost the same hole concentration as the maximum of the $T_c$ versus $n_h$ plot. The samples investigated herein have hole concentrations in the region of the maximal transition temperatures. Due to uncertainties of a possible small shift between the maxima of the $n_s$ versus $n_h$ and the $T_c$ versus $n_h$ curves it is very dangerous to assume a monotonic decrease of the penetration depth with increasing hole concentration in this range of hole concentration, as done above. Muon-spin experiments need to be done on the samples used in this work to investigate the penetration depth. Based on the results of these experiments, the suggested argumentation to explain the experimentally observed dependence of the critical current density on the hole concentration may be modified and extended. Apart from the uncertainty of the penetration depth, it may be wrong to assume a constant number of pinning centres in all samples of one series.

Actually, the observed experimental results can even be understood from a change in the number of pinning centres: From the neutron data it is known that the samples are all 6% thallium deficient. These thallium deficiencies cause a disorder of the structure and therefore improve the pinning. Argon annealing balances these deficiencies with oxygen deficiencies so that the structure of the material is less disordered and the pinning effect is smaller. According to the occupancy of the oxygen sites in the $TlO$ layers as given in table 4.5 and the observed corresponding critical current density values, this is exactly the case.

Even if the mentioned dependence of the critical current density on the apical $Cu-O$ bond length could not be explained as simply as attempted above, it fits well to the results reported by other groups [7, 8]. Kim et al.[7] pointed out that the small distance between $Cu-O$ conducting planes in $YBa_2Cu_3O_7$ may be the key to finding viable alternatives for achieving high critical current values. Liu et al.[8] observed a high critical current density in $(Tl_{0.5}Pb_{0.5})Sr_2Ca_2Cu_3O_9$. They believe that the three-dimensional character of this compound due to the enhancement of the superconducting coupling along the c-axis between the $Cu-O$ planes because of less insulating TlO layers than in the double thallium layer compounds is the reason for the increase in $J_c$ compared to the two-dimensional Tl-2223 and Tl-2212 systems. In this work the expansion in the c-parameter is much smaller than in their

case. This is appropriately reflected in the change of the $J_c$ values found here compared with the changes they obtained.

Summarizing it has been shown that the systematic change of the critical current density due to different annealing procedures can be understood as an effect of the change of the oxygen-stoichiometry, which is reflected in several changes of the microscopic structure.

## 4.4 Recent work on $Tl_2Ba_2Ca_3Cu_4O_{12}$

Very recently D. M. Ogborne and M. T. Weller succeeded in synthesising single superconducting phase $Tl_2Ba_2Ca_3Cu_4O_{12}$ and determined its structure by x-ray powder profile refinement. $Tl_2O_3$, $BaO_2$, $CaO$ and $CuO$ were mixed in the metal ratio 1.5 : 2.0 : 3.5 : 4.0 and thoroughly ground together in an agate pestle and mortar. The loose mixture was transferred to a gold tube which was crimped firmly shut. The tube was heated at $860^oC$ for 10 hours. The first sample prepared was quenched in air to room temperature. Samples prepared later were produced with the same solid state reaction but cooled slowly in the furnace and in one case annealed in oxygen afterwards. Data for profile refinement were only collected from the quenched sample over a 14 hour period in the two theta range $20 - 110^o$ with a step size of $0.02^o$. The peaks from the superconducting phase observed in the profile could all be indexed using the $I4/mmm$ space group common to all the double layer thallium cuprate superconductors. The c-parameter of 42Å is in good agreement with that given by previous workers and corresponds to the incorporation of an additional $CuO + Ca$ unit into the Tl-2223 structure. A reasonable model for this material can therefore be constructed from that of the Tl-2212 and Tl-2223 compounds. The refined atomic distribution gives reasonable bond distances for all atoms confirming the four copper layer model for $Tl_2Ba_2Ca_3Cu_4O_{12}$. The structure is shown in figure 4.17.

The transition temperature and the critical current density were measured with the same methods as described before. The results for all three samples prepared so far are shown in figures 4.18 and 4.19.

They show that the superconducting properties of the Tl-2234 compound are worse than those of the Tl-2223 samples. This has been reported by other workers before [16]. It can be explained by looking at the separation distance of the CuO layers in Tl-2212, Tl-2223 and Tl-2234. In the Tl-2223

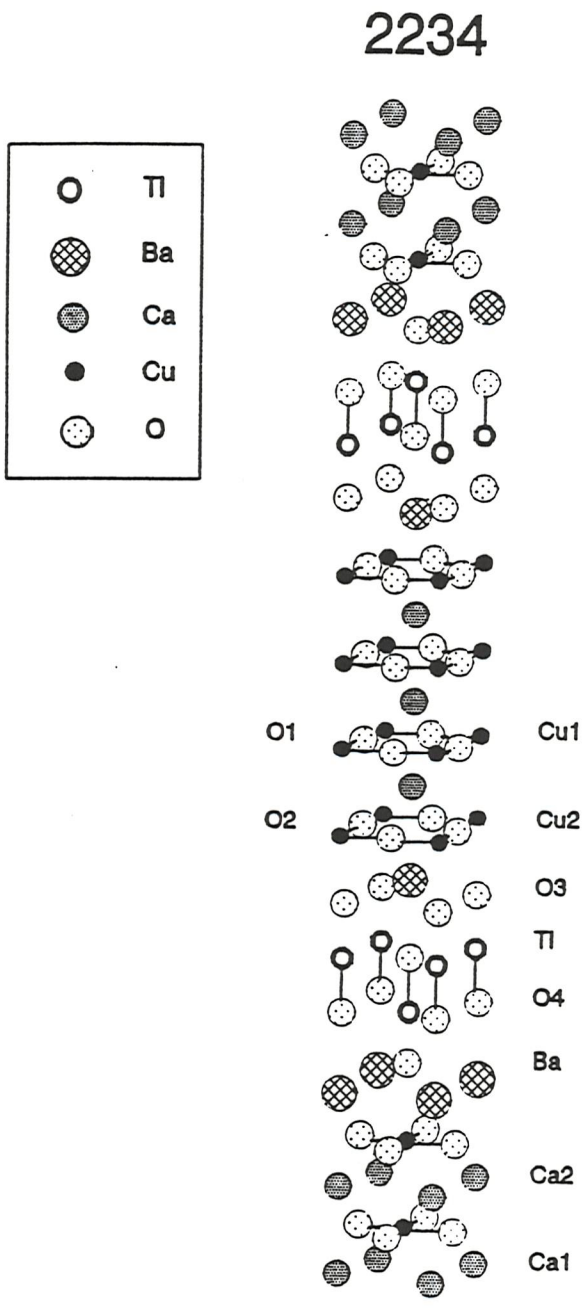


Figure 4.17: *Ball and stick representation of* $Tl_2Ba_2Ca_3Cu_4O_{12}$.

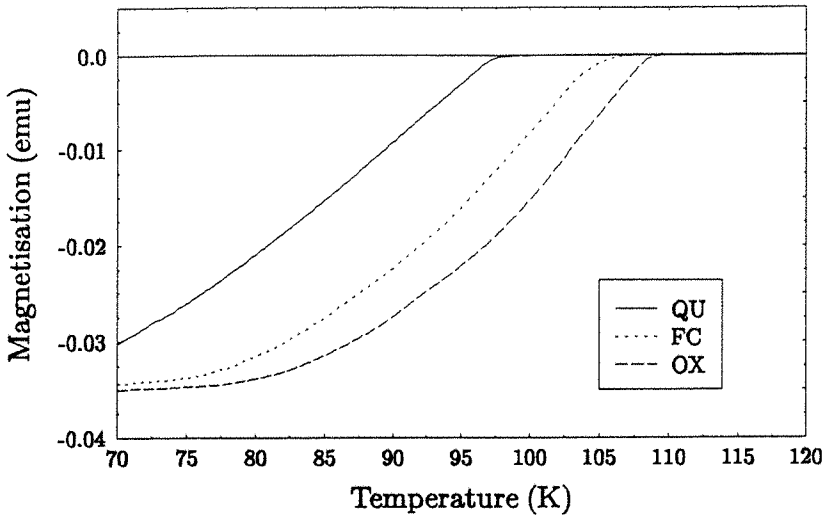


Figure 4.18: *Transition temperature of three Tl-2234 samples (Qu, FC, OX).*

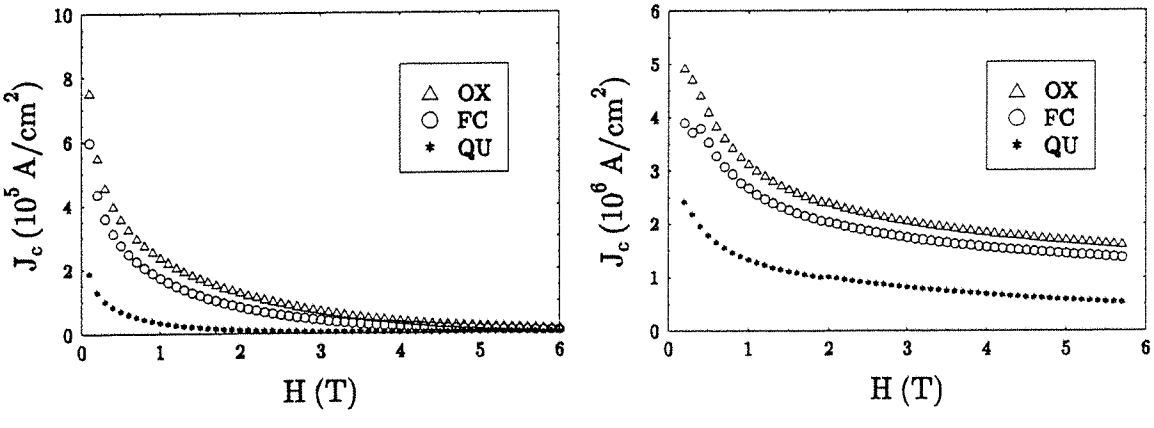


Figure 4.19: *Critical current density plotted as function of the of the applied field for three Tl-2234 samples at (a) 30K and (b) 4.2K.*

compound the highest $T_c$ and $J_c$ values have been observed. It contains three CuO layers which are separated by a distance of 3.19Å. The distance between the CuO layers is determined by the number of holes on them. The distance, and therefore in turn the hole concentration as well, in the Tl-2223 compound seems to have more or less the optimum value in order to obtain the best superconducting properties. The Tl-2212 compound with a interlayer-distance of 3.23Å seems to be overdoped with holes on the CuO layers, as a decrease of the hole concentration obtained by argon annealing leads to an improvement in the transition temperature. On the other hand the CuO layers in Tl-2234 are separated by a smaller distance (3.16Å) than those in Tl-2223. Here oxygen annealing led to an improvement of the superconducting properties as shown in figure 4.18. For further improvements the level of holes needs to be extended considerably. Preparation of high pressure oxygen annealed Tl-2234 samples is in process. The investigation of their structure and their superconducting properties will deliver a lot of work for following projects and may perhaps extend the results of this work to a general theory concerning the connections between them.

## 4.5 Conclusions

The magnetic studies made in this work on the double thallium layer compounds revealed so far unknown connections between the parameters of the preparation, the microscopic structure and the superconducting properties:

First, furnace cooling at the end of the solid state reaction turned out to give a more accurate structure of the ions and therefore better superconducting properties than quenching in air.

Second, both the transition temperature and the critical current density were found to depend strongly on the annealing parameters used. By analysing the neutron diffraction data, two main changes which occur in the material as a result of the various annealing treatments were observed. These are in the occupancy of the oxygen sites in the TlO layer and in the copper-oxygen apical bond length. They lead to a change of the hole concentration on the copper-oxygen planes.

The observed dependence of the transition temperature on the average Cu valence showed an inverted parabola shape, as predicted by theoretical models. Depending on the copper-oxidation state before the annealing

procedure, oxygen annealing led to higher or lower transition temperatures than argon annealing. In contrast to this, the critical current density was found to increase steadily with an increasing average Cu valence. High pressure oxygen annealing always resulted in a higher critical current density than argon annealing. This is believed to be due to changes in the penetration depth, which in turn change the vortex-vortex interaction. It can also be understood in terms of a balance between the thallium deficiencies and oxygen deficiencies. However, the attempt of optimising both superconducting properties of double layer thallium compounds using different annealing treatments may, according to these experimental results, often end as a compromise between the monotonic increase of the critical current density and the inverted parabola shape behaviour of the transition temperature with increasing oxygen content of the annealing gas.

# Bibliography


[1] D. M. Ogborne, M. T. Weller, and P. C. Lanchester, accepted for publication in Physica C

[2] D. M. Ogborne, M. T. Weller, and P. C. Lanchester, accepted for publication in Physica C

[3] R. S. Liu, J. L. Tallon, and P. P. Edwards, Physica C **182**, 119 (1991)

[4] T. Kaneko, H. Yamauchi, and S. Tamaka, Physica C **178**, 377 (1991)

[5] M. a. Subramanian et al. , Nature **332**, 420 (1988)

[6] Betty Ng and D. J. Newman, J. Sol. St. Commun. **77**, 287 (1991)

[7] T. Kaneko, K. Hamada, S. Adachi, and H. Yamauchi, "A Methode for Doping Tl-based Cuprate Superconductors with Holes." To be published in Physica C **197**, in press

[8] R. A. Rose, Ph.D. Thesis "Vortex motion and pinning in high-temperature superconductors"

[9] Tinkham, "Introduction to Superconductivity"

[10] A. I. Larkin and Yu. N. Ovchinnikov, J. low Temp. Phys. **34**, 409 (1979)

[11] P. W. Anderson, Phys. Rev. **112**, 1900 (1958)

[12] Betty Ng and D. J. Newman, Physica C **170**, 448 (1990)

[13] D. H. Kim et al., Physica C **177**, 431 (1991)

[14] R. S. Liu, D. N. Zheng, J. W. Loram, K. A. Mirza, A. M. Campbell, and P. P. Edwards, Appl. Phys. letters, in press

[15] D. M. Ogborne and M. T. Weller, accepted for publication in Physica C

[16] M. R. Presland, J. L. Tallon, P. W. Gilberd, and R. S. Liu, Physica C **191**, 307 (1992)

# Chapter 5

# Flux motion in $Tl_2Ba_2Ca_2Cu_3O_{10+\delta}$

## 5.1 Introduction

In contrast to the comparison of a variety of differently prepared thallium-based high temperature superconductors in the previous chapter, only one sample was used in this chapter to investigate the pinning force, the relaxation, the sweep-rate dependence of the critical current density and its dependence on the temperature. All these studies were made at the very beginning of this work. At that time only the first series had been prepared. Among this, the furnace cooled sample (Tl-2223/1pp/FC) had the best superconducting properties, as shown in chapter 4. Therefore it was decided to choose this sample for the investigations of this chapter. The aim of this part of the work was to investigate how far the theories presented in chapter 2 are applicable to thallium-based high temperature superconductors.

## 5.2 Pinning force measurements

The pinning force can easily be determined from the measured hysteresis loops by using the Bean model. Following the flux creep theory discussed in chapter 2, one would expect that the pinning force depends on the applied field as

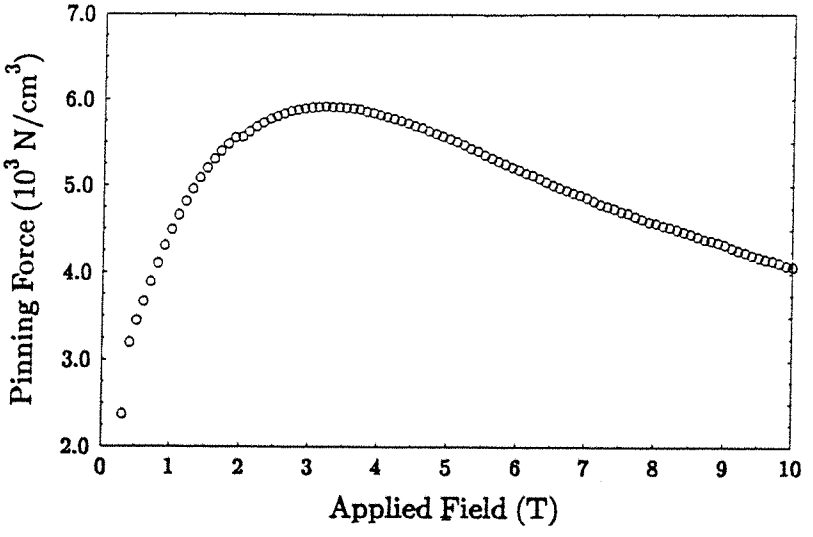


Figure 5.1: *Pinning force in Tl-2223/1pp/FC as calculated from a magnetic hysteresis loop performed at* $30K$ *with* $1mT/s$.

$$F_p(B) = \frac{k_B T\sqrt{B}}{1.07\sqrt{\Phi}\delta v}\text{arsinh}\left[\frac{E}{2.14\Omega_0\sqrt{\Phi B}}\exp\left(\frac{U_0}{k_B T}\right)\right] \tag{5.1}$$

This equation can be derived quite straight forwardly from equation 2.40. Equation 5.1 contains three variables which are not defined by the experimental conditions. They are $U_0$, $\delta v$ and $\Omega_0$ and are all determined by the properties of the vortex lattice. In order to obtain these parameters, equation 5.1 was fitted to the experimental data using the non-linear least square fitting routine described in chapter 3. An example of the experimental data is given in figure 5.1.

It shows the typical peak shape for type II superconductors [1]. It turned out to be a very tricky business to fit equation 5.1 to this data because of the field dependence of the fitting parameters. Dew-Hughes [2] proposed for pinning by normal precipitates or regions of reduced superconductivity, the field dependence of the pinning energy to be

$$U_0(B) = U(0)\left(1 - \left(\frac{B}{B^*}\right)^n\right) \tag{5.2}$$

where $B^*$ is another parameter which has to be determined by the fitting

program. The correlated volume $\delta v$ is also field dependent. The parameters given by the fitting program can not reflect the field dependence in a proper way and are therefore not physically sensible. It was decided to perform variable sweep-rate experiments in order to determine $U_0(B)$ and $\delta v(B)$ at fixed applied magnetic fields.

## 5.3 Variable sweep-rate experiments

When performing magnetic hysteresis loop measurements it was noticed that the width of the loop is dependent on the rate at which the magnetic field was swept round the loop. This was first reported by de Groot et al. [3]. Measuring the critical current density using magnetisation techniques is very common, but the sweep-rate $\beta = \frac{dH}{dt}$ used is not usually reported in published papers. Having discovered that this factor clearly affects the measured $J_c$-value, the dependence was studied in detail on the Tl-2223/1pp/FC sample. Magnetic hysteresis loops were performed as follows:

The sample was cooled in zero field from above $T_c$ to the required temperature of $30K$. The magnetic field was swept up to 6 Tesla, down to -2 Tesla and up again to +2 Tesla with the chosen sweep-rate. The sweep-rates used were $0.15mT/s$, $0.3mT/s$, $0.5mT/s$, $1mT/s$, $2mT/s$, $3mT/s$, $6mT/s$, $8mT/s$, $10mT/s$, $16mT/s$ and $20mT/s$. After each run the sample had to be warmed up above $T_c$ in order to avoid remanence trapped in the sample, as explained in the previous chapter.

A strong dependence of the screening current induced in the material on the sweep-rate was observed.

The sweep-rate dependence of the width of the magnetic hysteresis loops for certain values of the applied magnetic field is shown in figure 5.2. It was analysed in terms of the flux creep theory.

Starting from the flux creep relation for the electric field, a scaling equation describing the sweep-rate dependence of the loop width was derived in chapter 2.

$$\frac{\Delta M}{\Delta M^*} = \text{arsinh}\left(\frac{\beta}{\beta^*}\right) \tag{5.3}$$

where

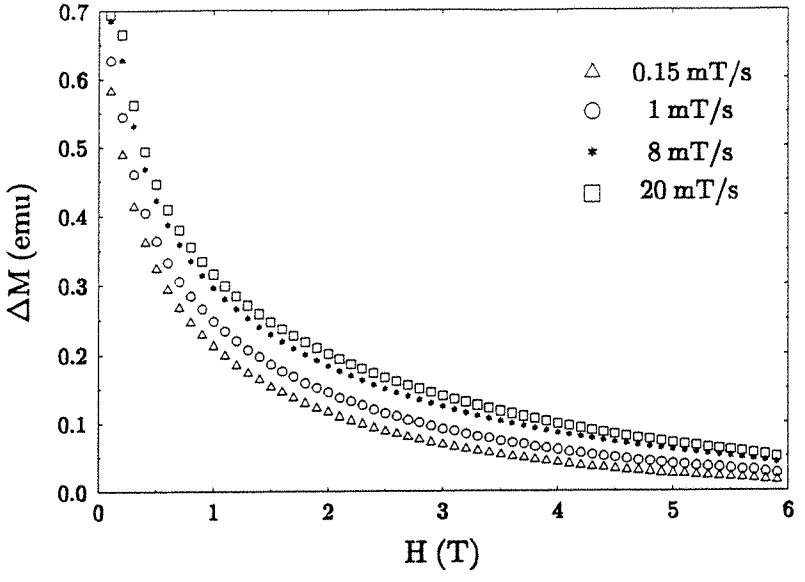


Figure 5.2: *Width of the magnetic hysteresis loop plotted as a function of the applied magnetic field for different sweep-rates.*

$$\Delta M^* = \frac{k_B T R}{15 B a_0 \delta v} \tag{5.4}$$

and

$$\beta^* = \frac{a_0 \Omega_0 B}{\pi R \exp\left(\frac{U_0}{k_B T}\right)} \tag{5.5}$$

The data was fitted to this equation using the non-linear least-square fitting routine described in chapter 3 with $\Delta M^*$ and $\beta^*$ as free parameters. The data scales quite well, as shown in figure 5.3.

The sweep-rate dependence of the critical current density can therefore be well described by following the flux creep theory. Fits to the data using the approximation of the logarithmic dependence (equation 2.47) resulting from the assumption $\Delta W \gg k_B T$ were as good as from the arsinh-dependence and gave the same fitting parameters. This reveals that the measurements were performed in the flux creep regime described in the Anderson-Kim model [4, 5]. Here the hyperbolic function can be approximated by an exponential function, as Beasley et al. did [6].

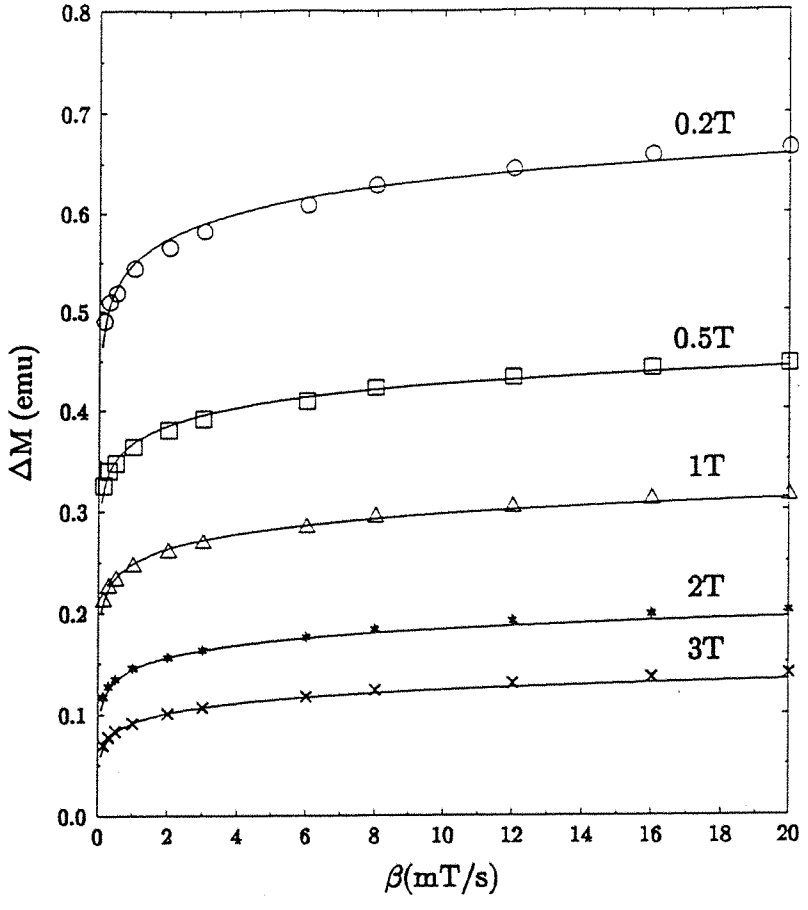


Figure 5.3: *Fit of equation 5.3 to the experimental data of the sweep-rate dependence of the width of the magnetic hysteresis loop plotted for different values of the applied magnetic field.*

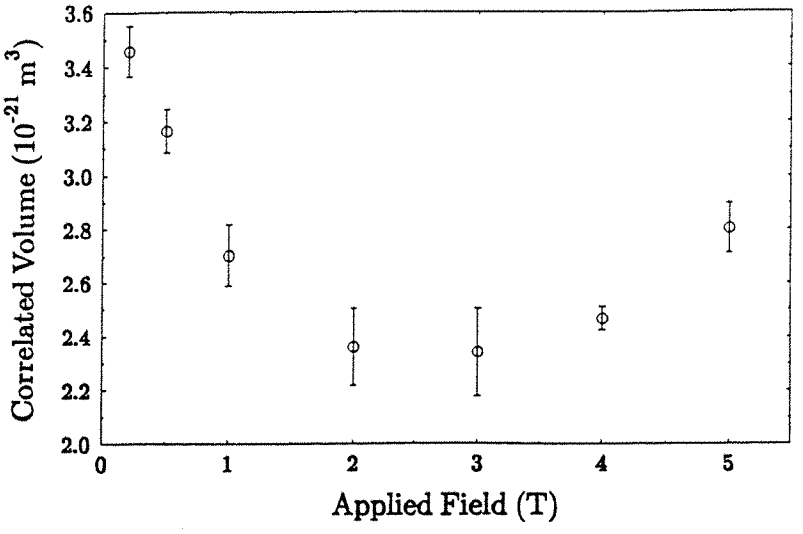


Figure 5.4: *Field dependence of the correlated volume $\delta v$ at $30K$ determined from variable sweep-rate experiments.*

The calculated values of the fitting parameters $\Delta M^*$ and $\beta^*$ were confirmed by several fits using different starting parameters and also by the values calculated from linear regression. Using equation 5.4 and 5.5, the pinning energy $U_0$ and the pinned volume $\delta v$ may be calculated from this parameters for certain values of the applied magnetic field. The results obtained are shown in figures 5.4 and 5.5.

The values of $\delta v$ are of the order of magnitude that one would expect. In [7, 8] it was argued that vortices in the Bi-2212 phase are like 2D-pancakes, and so the smallest possible size for a flux segment was calculated to be of the order of $10^{-24}m^3$ at $1T$. The values obtained here are above this level. The field dependence of the pinned volume is well reflected in the field dependence of the pinning force as one can see by looking at equation 5.1 and figure 5.1. The pinning force increases up to 3 Tesla and decreases afterwards. This corresponds to a decreasing value of $\delta v$ up to 3 Tesla and a following increase. Physically $\delta v$ corresponds in the flux creep theory to the inverse of the number of pinning centres. The observed $\delta v\,(B)$ behaviour means that the number of active pinning centres increases with field in the low field region, which in turn leads to a bigger pinning force, and decreases at higher fields, where the pinning force is smaller.

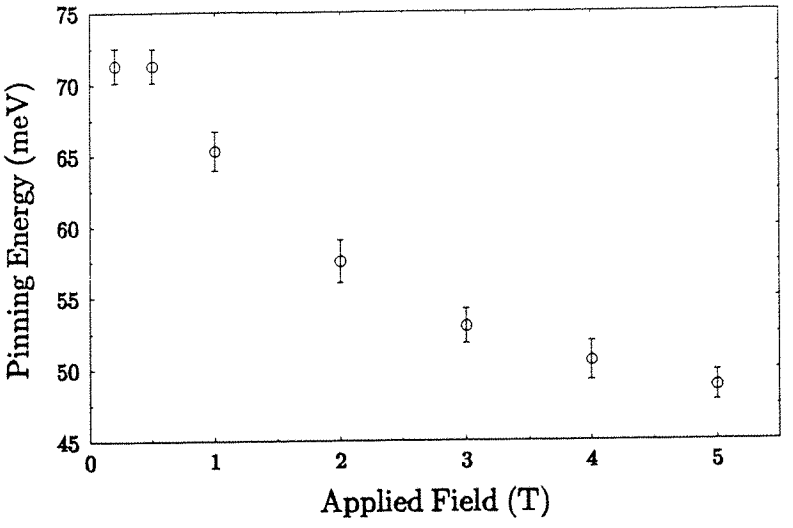


Figure 5.5: *Field dependence of the pinning energy $U_0$ at $30K$ according to the results of variable sweep-rate experiments.*

The values obtained for the pinning energy $U_0$ are within the range quoted by other people [11]. A decrease of the pinning energy with increasing applied magnetic field corresponds to the $U_0(B)$ behaviour proposed by Dew-Hughes [2].

## 5.4 Relaxation measurements

The decay of the magnetisation of a type II superconductor with time due to thermally activated flux motion over energy barriers was first calculated by Anderson [4]. Indeed this was one of the successes of the flux creep theory. Beasley et al. [6] derived for the case $\Delta W \gg k_B T$

$$M_i(t) = M_0 \left[1 - \frac{k_B T}{U_0} \ln(t + \Delta t)\right] \tag{5.6}$$

where $M_0$ is the magnetisation in absence of any flux creep and $\Delta t$ is the time after the beginning of the decay at which the measurement was started. In the VSM experiments $\Delta t$ depends on the time constant used in the VSM preamplifier. Here $\Delta t$ was measured repeatedly using a stopwatch and found to be eight seconds. The relaxation measurements were performed

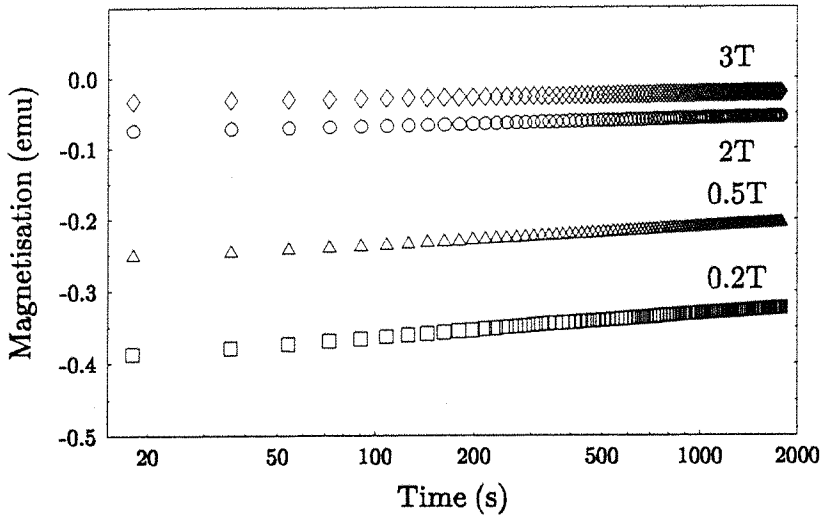


Figure 5.6: *Relaxation of Tl-2223/1pp/FC for different applied magnetic fields at* $30K$.

as follows: The sample (Tl-2223/1pp/FC) was cooled in zero field from above $T_c$ to $30K$. The required magnetic field was applied and the magnetisation measured over half an hour. The measurements were taken at $0.2T$, $0.5T$, $2T$ and $3T$. Figure 5.6 shows the characteristic logarithmic $M\,(t)$ dependence of the measured data.

The values of $U_0\,(B)$ calculated by using equation 5.6 are shown in figure 5.7.

The pinning energy values determined by variable sweep-rate experiments in the previous section ($U_{0_S}$) are also shown there. The differences of the values obtained here are very small, compared with the differences that other people found by using different measurement techniques [8]. However, the difference may be due to several small errors: The uncertainty in the fitting parameter $\beta^*$ causes a maximum possible error in the $U_{0_S}$ values of about 2%. The maximal possible error of $U_{0_R}$ due to the error in the fitting parameters is also in this range. A systematic error in $U_{0_S}$ may be caused by the rough estimation of $\Omega_0$ and the error in the grain-size.

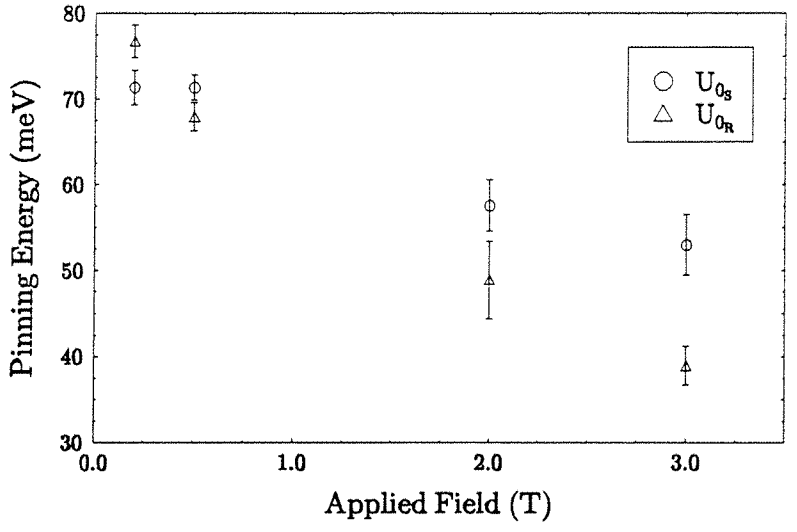


Figure 5.7: *Comparison of the field dependence of the pinning energy determined from relaxation measurements ($U_{0_R}$) and variable sweep-rate experiments ($U_{0_S}$).*

## 5.5 Direct comparison of magnetic hysteresis and magnetic relaxation

In the previous section corresponding values of the pinning energy $U_0$ at fixed fields were obtained using two different measurement techniques: magnetic relaxation and magnetic hysteresis. The theory of both methods is based on the Anderson-Kim theory of flux creep. In chapter 2 a direct correlation between sweep-rate dependence of the magnetisation and the magnetic relaxation with time was derived. Using the Anderson-Kim and the Bean model it was theoretically predicted that the relation

$$\frac{\partial \Delta M}{\partial \ln(\beta)} = -\frac{\partial \Delta M}{\partial \ln(t)} \tag{5.7}$$

is valid. From the data of the variable sweep-rate experiments and the relaxation measurements the values shown in table 5.1 were determined for $\frac{\partial \Delta M}{\partial \ln(\beta)}$ and $-\frac{\partial \Delta M}{\partial \ln(t)}$.

They are very similar but the values of the relaxation measurement are slightly smaller than those of the variable sweep-rate experiments. This was

| H | $\frac{\partial \Delta M}{\partial \ln(\beta)}$ | $\frac{\partial \Delta M}{\partial \ln(t)}$ |
|---|---|---|
| 0.2 T | 0.03669 | -0.02916 |
| 0.5 T | 0.02534 | -0.02162 |
| 2 T | 0.01753 | -0.00934 |
| 3 T | 0.01451 | -0.00560 |

Table 5.1: *Comparison of* $\frac{\partial \Delta M}{\partial \ln(\beta)}$, *and* $\frac{\partial \Delta M}{\partial \ln(t)}$.

also observed by Jirsa et al. [9] on $YBa_2Cu_3O_7$. They only suggested that Anderson's philosophy of thermally activated flux creep has to be modified. It is indeed true that some assumptions of the Anderson-Kim flux creep theory are too simplifying, as for example the assumed field independence of the pinning energy $U_0$. A possible explanation of a different pinning energy $U_0$ for the different measurement techniques used has been put forward by Maley et al. [10]. However, almost the same values of $U_0$ were obtained in the previous paragraphs from relaxation and variable sweep-rate experiments at fixed applied magnetic fields. This indicates that the observed difference between $\frac{\partial \Delta M}{\partial \ln(\beta)}$ and $-\frac{\partial \Delta M}{\partial \ln(t)}$ is due to a difference in $\Delta M_0$. $\Delta M_0$ is related to the critical current density $J_{c_0}$ before any flux creep occurs. It can not be determined directly from a real experiment. In the analysis of the variable sweep-rate experiment this value was not involved and in the relaxation measurement it has been taken into account that the actual measurement started with a delay after the beginning of the decay. The derivation of equation 5.7 depends essentially on the equality of $\Delta M_0$ in both cases. There has to be some doubt if this is really true in the experiments performed. It is hard to tell exactly how delays between the set-up of the experimental conditions and the actual measurement affect the results obtained in variable sweep-rate experiments, but estimates show that the $\Delta M_0$ values involved in the actual measured $\frac{\partial \Delta M}{\partial \ln(\beta)}$ values are indeed larger than those which are related to the critical current density before flux creep occurs. A more accurate investigation of this discrepancy would be useful, but could not be done in the frame of this work.

However, in the range of this experimental uncertainties it has been shown, that a direct correlation between magnetic relaxation with time and the sweep-rate dependence of the width of magnetic hysteresis loops can be

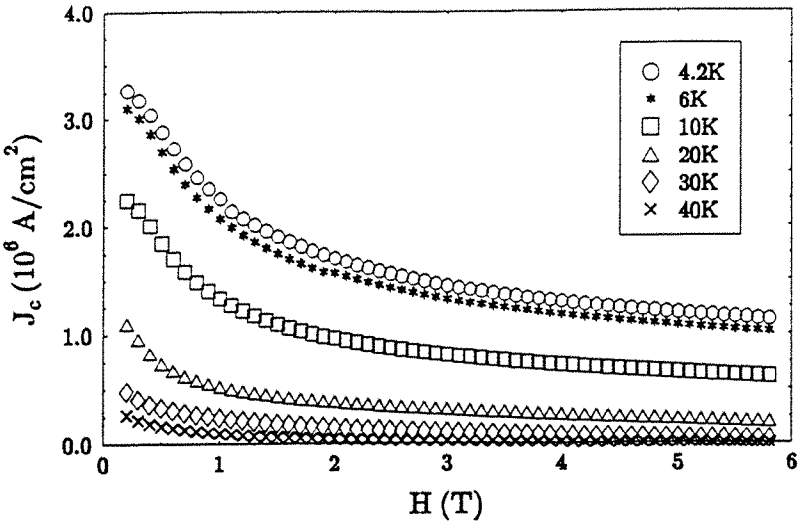


Figure 5.8: *Critical current density as a function of the applied magnetic field at different temperatures.*

made by following the Anderson-Kim theory of thermally activated flux creep in connection with the Bean model.

## 5.6 Variable temperature experiments

In order to investigate the temperature dependence of the critical current density, magnetic hysteresis loops were performed as described in the previous sections at $1.7K$, $3K$, $4.2K$, $6K$, $8K$, $10K$, $20K$, $30K$, $40K$, $50K$, $60K$, $70K$ and $77K$ with a sweep-rate of $20mT/s$ on the Tl- 2223/1pp/FCP sample. The critical current density was deduced from these, using the Bean model. The results are shown in figure 5.8.

In figure 5.9, the critical current density is plotted against the temperature at fixed fields. The data points at temperatures below $4.2K$ indicate that the temperature was not really stable at the required value. Therefore these points are excluded from the analysis.

As shown in chapter 2, Tinkham [12] predicted that, as a consequence of the Anderson-Kim model, the critical current density should vary with temperature as

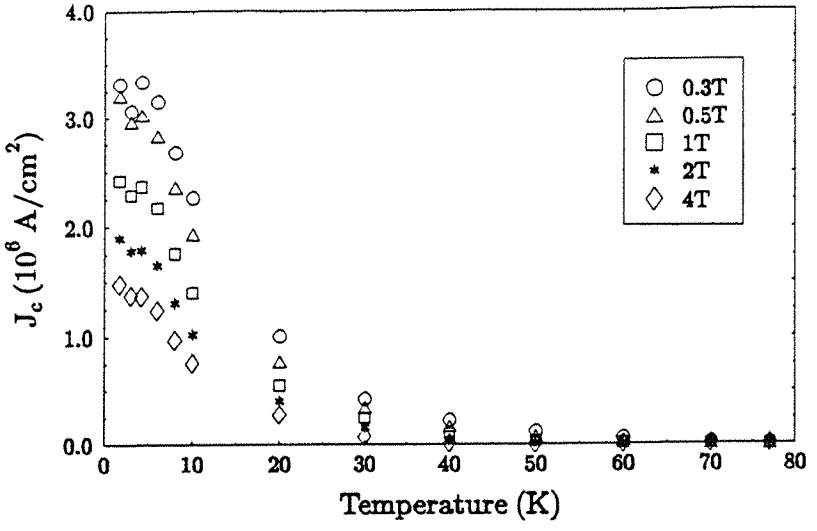


Figure 5.9: *Temperature dependence of the critical current density at several values of the applied magnetic field.*

$$J_c \propto 1 - \alpha(B)\,t - \beta t^2 \tag{5.8}$$

for $t = \frac{T}{T_c} \ll 1$.

An attempt was made to fit the measured data to this relation for values of t up to 0.5, but no proper fit could be obtained. This discrepancy was also observed by several other groups [13, 14, 15] who used magnetic methods to measure the critical current density. Senoussi et al. [13] found with magnetic measurements on single crystals of $YBa_2Cu_3O_{7-\delta}$ that the critical current density at fixed fields drops nearly exponentially over a wide range of temperature except near $T_c$ where $J_c(T)$ obeys a power law. The temperature variation of the critical current density at some fixed fields is depicted in figure 5.10 in a semilog scale. It also shows a nearly exponential drop of $J_c$ over a wide range of temperature. In contrast to this, transport measurements were found to confirm the behaviour predicted by Tinkham. This was reported for example by Mannhart et al. [16].

However, the exponential law of $J_c(T)$ observed by using magnetisation measurements cannot be explained by equation 5.8 deduced from the Anderson-Kim model. A possible explanation of the different results obtained by using different measurement techniques may be found in the different

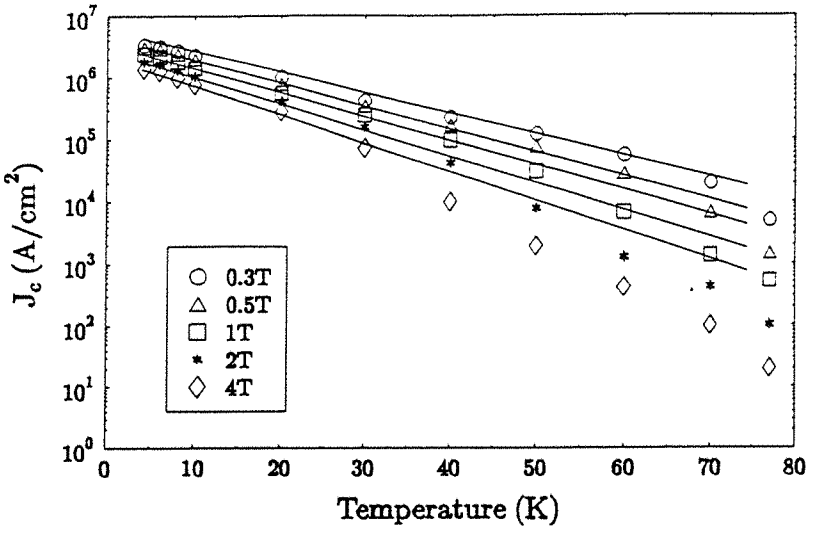


Figure 5.10: *Logarithmic fits to* $J_c(T)$.

current values in transport and magnetisation measurements, which are in the latter case typically one order of magnitude smaller.

## 5.7 Conclusions

The Anderson-Kim theory of thermally activated flux motion can, according to the experimental results of this chapter, fairly well describe flux motion in $Tl_2Ba_2Ca_2Cu_3O_{10+\delta}$ at $30K$ and fixed values of the applied magnetic field, but fails to explain the observed field and temperature dependence of the critical current density.

It has been observed in variable sweep-rate experiments and relaxation measurements that the values of the pinning energy $U_0$ and the correlated volume $\delta v$ were different for different values of the applied magnetic field. Anderson neglected these important factors in his theory. His assumptions are too simplifying to explain the field and temperature dependence of the critical current density in thallium-based high temperature superconductors. More recent models of flux motion take the field and temperature dependence of the pinning energy $U_0$ and the correlated volume $\delta v$ into account, but were not applicable to the experiments done in this work because of different temperature and field regimes. A new comprehensive theory is still lacking.

# Bibliography


[1] D. P. Hampshire, J. A. S. Ikeda, and Y. M. Chiang, Phys. Rev. B **40**, 8818 (1990)

[2] D. Dew-Hughes, Philosophical Mag. **55**, 459 (1987)

[3] P. A. J. de Groot, C. E. Meats, G. P. Rapson, J. R. Grasmeder, P. C. Lanchester, M. T. Weller, J. Phys. F **18**, L123 (1988)

[4] P. W. Anderson, Phys.Rev. Lett. **9**, 309 (1962)

[5] Y. B. Kim, C. F. Hempstead, and A. R. Strnad, Phys. Rev. Lett. **9**, 306 (1962)

[6] M. R. Beasley, R. Labusch, and W. W. Webb, Phys. Rev. **181**, 682 (1969)

[7] P. H. Kes, J. Aarts, V. M. Vinokur, and C. J. van der Beek, Phys. Rev. Lett. **64**, 1063 (1990)

[8] J. R. Clem, Phys. Rev. B **43**, 7837 (1991)

[9] M. Jirsa, L. Půst and J. Kadlecová, J. Mag. and Mag. Materials **101**, 105 (1991)

[10] M. P. Maley, J. O. Willis, H. Lessure, and M. E. McHenry, Phys. Rev. B **42**, 2639 (1990)

[11] R. A. Rose ,"Vortex motion and pinning in high-temperature superconductors", Ph.D. thesis

[12] M. Tinkham, Helvetica Physica Acta **61**, 443 (1988)

[13] S. Senoussi, M. Ousséna, G. Collin, and I. A. Campbell, Phys. Rev. B **37**, 9792 (1988)

[14] W. Guan, conference preprint

[15] E. M. Gyorgy, R. B. van Dover, S. Jin, R. C. Sherwood, L. F. Schneemeyer, T. H. Tiefel, and J. V. Waszczak, Appl. Phys. Lett. **53**, 2223 (1988)

[16] J. Mannhart, P. Chaudhari, D. Dimos, C. C. Tsuei, and T. R. McGuire, Phys. Rev. Lett. **61**, 2476 (1988)

# Chapter 6

# Summary

This thesis describes research on the magnetic properties of thallium-based high temperature superconductors belonging to the homologous series $Tl_2Ba_2Ca_{n-1}Cu_nO_{2n+4}$ $(n = 2, 3, 4)$. These materials are characterised by a layered structure, consisting of alternating superconducting CuO layers and TlO layers. Amongst the HTS the highest transition temperatures are found for these thallium-based cuprates, but the maximum current that they can carry without resistance is relatively small compared with critical current values of other high temperature superconductors like $YBa_2Cu_3O_7$. In order to use thallium-based materials for applications, this property has to be improved. The main purpose of this work was to investigate the effect of different preparation procedures on the intrinsic pinning of flux lines, which determines the critical current. First, existing theories of flux motion were presented. Anderson and Kim developed the model of thermally activated flux creep. This has been modified for different specific temperature and field regimes by several authors. Charles Bean derived a relation between the critical current density of conventional superconductors and the magnetisation measured in a magnetic hysteresis loop. Even so that this is a rather simple model in which the complex structure of high temperature superconductors is not reflected, it provides a possibility to investigate changes in the critical current density with the equipment available for this work. The equipment consisted basically of a 12 Tesla Oxford-Instruments vibrating sample magnetometer and a Joel-JSM-6400 scanning electron microscope. The thallium samples investigated herein were prepared by D. M. Ogborne. Solid state reactions yielded samples of single phase $Tl_2Ba_2Ca_1Cu_2O_{8+\delta}$,

$Tl_2Ba_2Ca_2Cu_3O_{10+\delta}$ and $Tl_2Ba_2Ca_3Cu_4O_{12+\delta}$. Afterwards these were annealed under different conditions. Powder x-ray and neutron diffraction experiments revealed that the main change which occurred in the material as a result of the various annealing treatments was in the occupancy of the oxygen site in the TlO layers and in the copper-oxygen apical bond length. Both affect in turn the hole concentration on the copper-oxygen planes. Furthermore the structure of the samples was investigated using scanning electron microscopy which provided essential information about the shape and the size of the grains.

Using the 12 Tesla Oxford-Instruments vibrating sample magnetometer, the transition temperature was found to follow an inverted parabola shape dependence on the oxygen content of the sample. The oxygen content of the sample was changed systematically by the annealing treatment and determines the hole concentration on the copper-oxygen planes, as found in the neutron experiments. The critical current density of all differently prepared samples was calculated from magnetic hysteresis loops on the basis of the Bean model. The magnetic hysteresis loops were performed at $4.2K$ and $30K$ with a sweep-rate of $20mT/s$. A monotonic increase of the critical current density with increasing oxygen content was observed in all investigated series. The experimental results have been discussed considering various aspects. It turned out that an explanation based on the connection between the hole concentration on the copper-oxygen planes and the vortex motion requires more detailed information about the relation between the hole concentration and the penetration depth. Muon-spin rotation experiments are necessary to ensure the proposed argumentation. The results of the neutron data indicate another possible explanation which is based on the thallium deficiencies. Annealing of the samples in an argon atmosphere balances these according to the observed occupancy of the oxygen site in the TlO layers. This leads to a less disordered structure and therefore to a smaller pinning effect which is indeed reflected in the experimental results.

However, the comparative studies of differently prepared thallium-based high temperature superconductors showed that an increase in the hole concentration on the copper-oxygen planes improves the critical current density. Looking at the dependence of the transition temperature and the critical current density on the annealing parameters, the results of this work indicate that the attempt of optimising both superconducting properties in double thallium layer compounds by applying different annealing treatments may

often end as a compromise.

Apart from the studies of differently prepared samples, flux motion in one specific $Tl_2Ba_2Ca_2Cu_3O_{10+\delta}$ sample has been investigated using various methods:

The pinning force was measured as a function of the applied magnetic field at a fixed temperature and a fixed sweep-rate. An attempt to fit the field dependence of the pinning force that was predicted by the Anderson-Kim model to the data remained unsuccessful. It was presumed that this could be explained by the dependence of the fitting parameters $U_0$ and $\delta v$ on the applied magnetic field.

Variable sweep-rate experiments indeed confirmed the presumption. Magnetic hysteresis loops were performed with different sweep-rates at $30K$. $U_0$ and $\delta v$ were calculated on the basis of the Anderson-Kim model at certain values of the applied magnetic field. Both turned out to vary with the field, as presumed. Their field dependence corresponded well with the observed field dependence of the pinning force.

Relaxation measurements were performed at $30K$ with four different values of the applied magnetic field. The results showed a logarithmic $M(t)$-dependence and were analysed using the Anderson-Kim model. The determined $U_0$ values were roughly the same as those obtained from the variable sweep-rate experiments, if one considers the possible range of error. A direct correlation between magnetic hysteresis and magnetic relaxation was derived in the theory part from the Anderson-Kim and the Bean-model. The experimental results gave a slight discrepancy with the theoretically predicted equation. This is believed to be due to experimental restrictions of the equipment but has to be investigated in more details.

Furthermore magnetic hysteresis loops were performed at various temperatures with a fixed sweep-rate. The critical current density was calculated from these. Tinkham derived the temperature dependence of the critical current density based on the Anderson-Kim model. His relation could not be fitted to the experimental data. It was found, that the critical current density at fixed fields drops exponentially over a wide range of temperature except near $T_c$, where $J_c(T)$ obeys a power law.

The last part of this work showed therefore that the Anderson-Kim model could describe flux motion in $Tl_2Ba_2Ca_2Cu_3O_{10+\delta}$ at $30K$ and at fixed values of the applied field, but failed to describe the temperature and field dependence of the critical current. This is due to too simplifying assumptions about

the pinning energy $U_0$ and the nature of the flux bundles. More recent models of flux motion involve these factors in their theories. A comprehensive theory that is able to describe flux motion in high temperature superconductors over a wide range of temperatures and fields is still lacking.

A lot more aspects have to be experimentally investigated to provide information for a theory which may suggest how to obtain HTS with superconducting properties, that allow their use for applications. The systematic collaboration of the Physics, Chemistry and Cryogenics Departments here in Southampton produces promising results in this field.